Intrahalocline eddies in the Amundsen Basin observed in the distributed network from the MOSAiC expedition

Alejandra Quintanilla-Zurita[1], Benjamin Rabe[1], Claudia Wekerle[1], Torsten Kanzow[1,2], Ivan Kuznetsov[1], Sinhue Torres-Valdes[1], Enric Pallàs-Sanz[3], and Ying-Chih Fang[4]

[1]Alfred-Wegener-Institut Helmholtz-Zentrum für Polar- und Meeresforschung, Bremerhaven, Germany
[2]Faculty of Physics, University of Bremen, Bremen, Germany.
[3]Centro de Investigación Científica y de Educación Superior de Ensenada, Baja California, Mexico
[4]Department of Oceanography, College of Marine Sciences, National Sun Yat-sen University, Kaohsiung, Taiwan

Correspondence: Alejandra Quintanilla-Zurita (alejandraquintanillaz@gmail.com)

Abstract. Hydrographic and velocity observations from the Multidisciplinary Drifting Observatory for the Study of Arctic Climate (MOSAiC) expedition (2019–2020) reveal the presence of nine intrahalocline eddies (IHEs) in the Amundsen Basin during the winter drift of the Distributed Network (DN). Despite their relevance for Arctic stratification and mixing, IHEs in the Amundsen Basin remain poorly documented. Our study addresses this gap by providing the first detailed characterisation based on coordinated in situ hydrographic and velocity observations during wintertime. Eddies were identified as isopycnal displacements in Ice-Tethered Profiler (ITP) data. Additionally, by assessing rotational velocity signatures from Acoustic Doppler Current Profiler (ADCP) measurements, we applied a centre-detection method based on maximum swirl velocity (MSV). Nine anticyclonic eddies were observed, with radii ranging from 3.7 to 8.4 km and vertical extents between 23 and 80 m. Most eddies exhibited solid-body rotation in their cores, with maximum azimuthal velocities of up to 0.28 ms^{-1} and localised shallowing of the mixed layer by over 10 m. Water mass analysis showed that the eddy cores contained Eurasian halocline waters with consistent anomalies in temperature, salinity, and density relative to surrounding profiles, allowing us to infer pre-existing stratification conditions and offering clues to their origin. The observed eddy scales lie close to or slightly below the first baroclinic Rossby deformation radius of approximately 6.9 km, placing them in the (sub)mesoscale dynamical regime and suggesting a transitional balance where both geostrophic and cyclogeostrophic effects may be relevant. The MSV method yields systematically larger eddy radius estimates up to 25% greater than traditional detection techniques that rely on velocity profiles or isopycnal displacements alone. This correction to the radius is essential, as it provides a more realistic measure of eddy size and dynamics under ice-covered conditions and could improve comparability across under-ice eddy studies. Although specific generation mechanisms remain uncertain, thermohaline signatures suggest that shallow local convection and baroclinic instability play a role in their formation. Our results provide new insights into the dynamics of under-ice eddies and their potential impact on Arctic oceanography and climate processes, addressing essential gaps in understanding polar mesoscale dynamics.

1 Introduction

The global ocean surface is densely populated by mesoscale eddies. These can be tracked through satellite-derived sea surface height anomalies (Chelton et al., 2011). However, much less is known about the subsurface eddies below the mixed layer in sea ice-covered regions, particularly in the Arctic Ocean. Intrahalocline eddies (IHEs)— similar to intrathermocline eddies (Dugan et al., 1982)—are coherent features. They range from submesoscale to mesoscale and sit within the halocline, generally just below the mixed layer (e.g., Kuzmina et al., 2008). Unlike their open-ocean counterparts, Arctic IHEs evolve within a strongly stratified, ice-covered environment. Their significance lies in their ability to modify upper-ocean stratification, modulate mixed-layer properties, and alter cross-basin transport pathways, thereby influencing the broader Arctic Ocean circulation. These subsurface features have also been linked to the lateral redistribution of heat, salt, freshwater, nutrients, and biogeochemical tracers, and may further modulate vertical exchange and sea-ice–ocean feedbacks (e.g., Timmermans et al., 2008; Lenn et al., 2022; Von Appen et al., 2022).

The Arctic Ocean displays some of the smallest dynamic scales globally, with the first baroclinic Rossby radius of deformation typically about 10 km (Nurser and Bacon, 2014). Finer-scale analyses, however, suggest the limit may be even smaller, which makes sampling mesoscale structures beneath the sea ice especially challenging. This small scale complicates the detection of IHEs, as their diameters may approach or fall below this length. To reflect this, we refer to these features as (sub)mesoscale eddies, acknowledging that their scales may span both mesoscale and submesoscale regimes—especially in the Arctic, where overlapping dynamical processes make precise scale separation difficult to define (Della Penna and Gaube, 2019). In this study, we focus on the Amundsen Basin, a key yet sparsely sampled region of the central Arctic Ocean where IHEs remain poorly documented. The Amundsen Basin is the deepest part of the Arctic Ocean, reaching depths of 4500 m, bounded by the Lomonosov and Gakkel ridges (Figure 1a). Its upper water column is strongly stratified, with a mixed layer extending to 50 m depth in winter, temperatures close to the freezing point ($\approx$ -1.8 °C) and salinity below 33, underlain by a sharp halocline that separates the mixed layer from the warmer and saltier Atlantic water located at $\approx$200 m depth (Rudels et al., 1996; Polyakov et al., 2020). The Transpolar Drift, the primary surface current in the central Arctic Ocean, influences the Amundsen Basin by transporting sea ice and freshwater from the Siberian shelves to the Fram Strait, shaping the large-scale structure of the halocline (Morison et al., 2012; Rabe et al., 2014).

In general, eddies are characterised by a maximum vertical displacement of isopycnals at their centre, consistent with geostrophic balance, and horizontal velocities reach a minimum at the eddy centre and increase radially outward within the solid-body core (Zhao and Timmermans, 2015). IHEs represent a subset of these features, characterised by distinct thermohaline properties relative to ambient waters (Kostianoy and Belkin, 1989). Anticyclonic IHEs typically exhibit domed isopycnals above and depressed isopycnals below. The opposite vertical structure is theoretically expected for cyclonic subsurface eddies: depressed isopycnals above and domed isopycnals below (e.g., McGillicuddy Jr, 2015; Zhao et al., 2014), although such features have not been documented as IHEs in the Amundsen Basin and were not observed in our dataset. The velocity field of these eddies exhibits a subsurface maximum of azimuthal velocity and approximate azimuthal symmetry (Thomas, 2008). These features belong to the global class of density-trapped subsurface vortices commonly termed intrathermocline eddies or

subsurface lenses (e.g., McWilliams, 1985, 1988; Chaigneau et al., 2011; Dilmahamod et al., 2018). In the Arctic Ocean, where stratification is predominantly halocline-controlled, similar features have been described as IHEs (e.g., Zhao et al., 2018; Fine et al., 2018). We therefore adopt this terminology to reflect the strong and shallow halocline characteristic of the Amundsen Basin.

Previous studies of such eddies, mainly in the Canada Basin (e.g., Aagaard and Carmack, 1989; Manley and Hunkins, 1985; Timmermans et al., 2008; Zhao et al., 2014), contrast with sparse evidence from the Eurasian Basin, mostly from limited mooring observations (Polyakov et al., 2012; Woodgate et al., 2001). Zhao et al. (2014) identified 39 eddies containing Eurasian Basin water from a decade of Ice-Tethered Profiler (ITP) data, but most were found on the Canadian side, rarely in the Amundsen Basin, confirming that the region remains poorly sampled and characterised. Their study showed that these Arctic subsurface eddies are predominantly anticyclonic, with radii of 3.5-7 km, core depths of 54–150 m, mean azimuthal velocities of 0.05–0.22 ms^{-1}, and Rossby numbers of 0.07–0.63. Beyond their structure, these eddies redistribute water and heat within the halocline, affecting halocline maintenance, mixed layer properties, and upper-ocean heat content in a changing Arctic, and thereby modulate vertical heat fluxes toward the sea ice, lateral exchange between boundary currents and the basin interior, and the storage and release of heat and freshwater anomalies on basin scales (e.g., Von Appen et al., 2022; Lenn et al., 2022). Recent observations from the MOSAiC expedition (Rabe et al., 2022) also detected eddy-like velocity anomalies in the Amundsen Basin using velocity data in the Central Observatory (Schulz et al., 2024), although these provided only partial information about their structure and origin.

High-resolution modelling studies, such as those by Müller et al. (2024) and Li et al. (2024), using kilometre-scale simulations (e.g. FESOM2, Danilov et al., 2017), suggest that the Eurasian Basin is densely populated by mesoscale eddies, with eddy activity closely linked to baroclinic instability of the Atlantic Water boundary current and sea ice dynamics. Complementing these model-based insights, Kuznetsov et al. (2024) reconstructed the ocean state from MOSAiC observations, providing a detailed view of subsurface dynamics and identifying numerous cyclonic and anticyclonic eddies beneath the ice, most of which appear to be in a quasi-steady state. Together, this evidence highlights strong motivation for observational characterisation of IHEs in the Eurasian Basin.

This paper aims to provide a detailed characterisation of wintertime intrahalocline (sub)mesoscale eddies in the Amundsen Basin, using MOSAiC hydrographic and velocity data to investigate their dynamics, thermohaline properties, formation processes, and variability among individual eddies.

2 Methods

2.1 Data

The data used in this study were collected during the MOSAiC expedition (Nicolaus et al., 2022; Rabe et al., 2022). In particular, we use data from the Distributed Network (DN) (Rabe et al., 2024), which was installed around the Central Observatory (CO), where the *Polarstern* was anchored to the ice. We restrict our analysis to the winter period from October 19, 2019 to March 15, 2020 (for daily drift locations see Figure 1a). The DN consisted of several autonomous ice-tethered systems de-

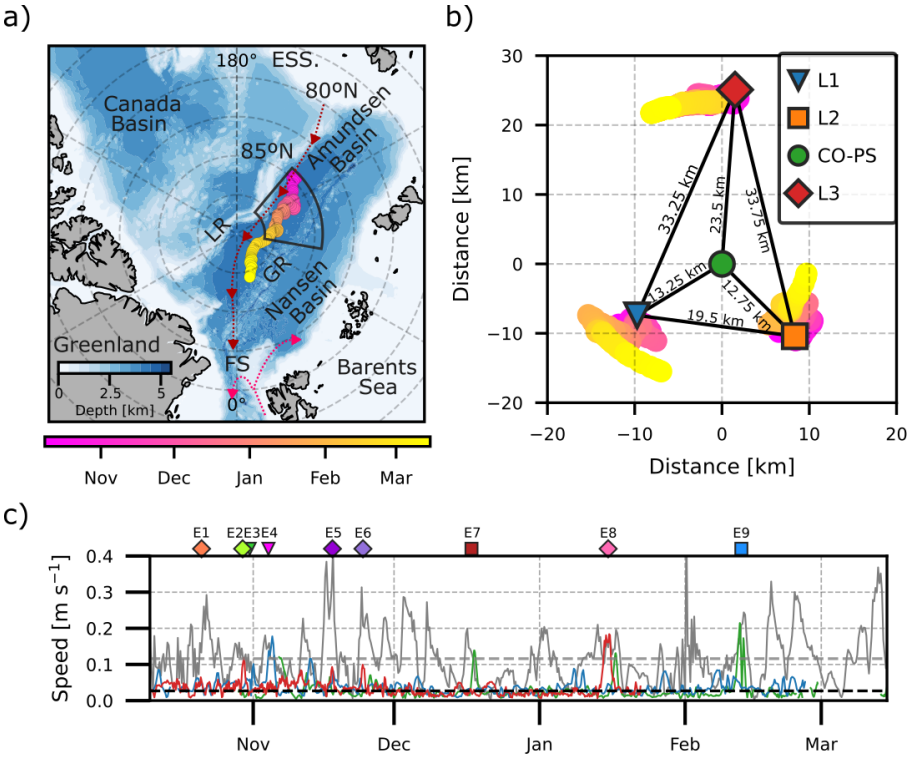

Figure 1. (a) Drift track of the Central Observatory (CO) on the MOSAiC expedition from October 19 2019 to March 15 2020. The blue scale represents the bathymetry ($\times 10^3$ m), based on the International Bathymetric Chart of the Arctic Ocean (Jakobsson et al., 2008). Schematic arrows indicate the major upper-ocean circulation pathways: the Warm Atlantic Water Boundary Current (pink) and the Transpolar Drift (red). Key bathymetric and geographic features are labelled, including the Lomonosov Ridge (LR), Gakkel Ridge (Gk), Fram Strait (FS), and the East Siberian Shelf (ESS). The black polygon in panel a shows the main area of study. (b) Initial spatial configuration of the L-sites relative to the CO–PS on 19 October 2019 (markers), and their subsequent relative displacements from 19 October 2019 to 15 March 2020 (colour-coded positions). The colour scale matches that of panel (a), indicating the date along the drift trajectory. (c) Drift speed of the CO (grey line) and the mean current speed averaged over the available ADCP depth range at CO-PS (green line), L1 (blue line), and L3 (red line). The dashed grey and black lines show the mean drift and mean current speed, respectively. The timing of each detected eddy (E1–E9) is indicated at the top of the panel.

signed to collect Arctic Ocean properties at different temporal and spatial scales. The DN includes both fixed-depth time series data and vertical profiles. Although fixed-depth sensors provide high temporal resolution data (on the order of minutes) and capture eddy signatures (Hoppmann et al., 2022), they are unsuitable for detailed characterisation of individual eddies. This is because fixed-depth data do not capture the full vertical structure of IHEs, which require vertical profiling to resolve their thermohaline and velocity structure. Therefore, this study uses exclusively vertical profile data to analyse the structure and dynamics of wintertime IHEs. We focus on the three instrument deployment locations, termed L-sites, which were positioned

Table 1. Instrumentation and sampling characteristics for each Distributed Network (DN) site.

Location site	Platform (Buoy system)	Sensor type	Deployment period	Time between profiles [h]	Depth range [m]	Depth bin size [m]
L1	ITP 111	CTD	07-10-2019 – 11-06-2020	6–18	10–200	1
L1	AOFB	ADCP	07-10-2019 – 27-02-2020	3	12–80	2
L2	ITP 94	CTD	08-10-2019 – 29-07-2020	6–24–6–36	10–200	1
CO-PS	AOFB	ADCP	14-10-2019 – 19-03-2020	2	12–80	2
L3	ITP 102	CTD	11-10-2019 – 31-01-2020	3	10–200	1
L3	AOFB	ADCP	10-10-2019 – 22-01-2020	2	10–80	2
CO-PS	Polarstern	CTD	14-11-2019 – 02-20-2020	-	1–4000 (Bottom)	1
CO-PS	Polarstern	ADCP	28-10-2019 – 04-06-2020	1/60	25–200	8

AOFB = Autonomous Ocean Flux Buoy, CO-PS = Central Observatory-*Polarstern*, ITP = Ice-Tethered Profiler

at a distance of approximately 12–24 km around the CO (Figure 1b). At the L-sites, Ice-Tethered Profilers (ITPs) (Krishfield et al., 2008; Toole et al., 2011) provided Conductivity, Temperature and Depth (CTD) measurements, and Autonomous Ocean Flux Buoys (AOFBs) (Stanton et al., 2012) equipped with Acoustic Doppler Current Profilers (ADCP) measured horizontal velocity. We also used CTD measurements from the surface to the ocean floor and velocity data from the *Polarstern* shipboard ADCP. All datasets were used in their publicly released, quality-controlled form from the official MOSAiC data products, including the ITP (Toole et al., 2016), the *Polarstern* sADCP (Tippenhauer and Rex, 2020), the AOFB (Stanton and Shaw, 2023), and the *Polarstern* CTD (Tippenhauer et al., 2023). No additional corrections, averaging, or interpolation were applied. Only the velocity data were smoothed with a half-day low-pass filter to reduce high-frequency noise while retaining eddy-scale variability. This was done to remove the short-period noise while preserving temporal variability at time scales expected for (sub)mesoscale eddies, which typically last several days. The MLD was defined as the first depth at which the Brunt–Väisälä frequency anomaly, ΔN, between successive measurements exceeded $3 \times 10^{-4} s^{-2}$. This threshold was selected following a visual inspection of all available profiles, as it reliably captured the transition from the mixed layer to the onset of the halocline during the MOSAiC drift. All thermodynamic variables, including density, N, and derived quantities, were computed using TEOS-10 through the GSW Python toolbox (McDougall and Barker, 2011).

The three L-sites were instrumented with ITPs and AOFB-mounted ADCPs, each operating with different profiling intervals and vertical sampling ranges (Table 1). Because all platforms drifted with the sea ice, the horizontal spacing between consecutive profiles depended on both drift speed and profiling interval, ranging approximately from 1 to 10 km, with the L3 ITP providing the smallest spacing and L2 the largest. The L1 and L2 sensors remained operational throughout the winter and drifted toward the Fram Strait, whereas the L3 sensors ceased operation on 31 January 2020 following an ice-ridging event. The L2 ADCP did not return usable data due to early technical failure, and when L2 and the Central Observatory were aligned, velocity measurements were supplemented using the *Polarstern* shipboard ADCP.

2.2 Eddy detection

In this study, the DN moved with the sea ice at a mean drift speed of $0.11\ \mathrm{m\ s^{-1}}$, while the underlying ocean current below the mixed layer had an average speed of $0.02\ \mathrm{m\ s^{-1}}$ (Figure 1c). Because ice drift is an order of magnitude faster than ocean currents, the ice-tethered platforms move quickly relative to the ocean features beneath them. The DN geometry also remained stable during the drift (Figure 1b), with inter-platform distances changing only slightly and always exceeding the expected diameter of Arctic intrahalocline eddies. This large difference in speeds and the absence of significant deformation or rotation of the array justifies the quasi-synoptic assumption, which means that measurements from the ice-advected platforms can be considered as near-instantaneous snapshots ("frozen fields") of the slower-evolving ocean eddies (Manley and Hunkins, 1985; Krishfield et al., 2008). Furthermore, the analysis was restricted to DN trajectories that followed approximately linear paths during each eddy encounter, thereby minimising potential geometric biases arising from the relative motion between the platform and a propagating eddy. This interpretation agrees with observations that Arctic eddies propagate at speeds roughly an order of magnitude slower than the sea ice drift (von Appen et al., 2018).

To identify eddies, we follow the methodology suggested by Timmermans et al. (2008) and Zhao et al. (2014). Eddies were first recognised in the ITP profiles by visually detecting coherent vertical displacements of isopycnals across several consecutive casts, reflecting the eddy's spatial structure as the drifting platform crosses it. In the case of the anticyclonic IHEs, the only type of eddies detected in our dataset, the upper part of the eddy shows a convex upward doming of isopycnals, whereas the lower part exhibits a concave downward displacement, producing opposite slopes above and below the core. In a second step, we analyse the velocity profiles measured by the ADCPs and look for the characteristic eddy velocity anomaly, with two local maxima in horizontal speed, one on each side of the isopycnal displacement centre. Figure 2 illustrates this two-step identification using the hydrographic displacement and the associated speed anomalies. E8 (a) at L3 was sampled with the smallest horizontal spacing between profiles, whereas E9 (b) at L2 had the largest spacing. These examples show how eddy-like structures are recognised from the combined ITP–ADCP signal before applying dynamical consistency tests.

The last step in confirming that an eddy-like structure is in fact a rotating eddy is to verify that the velocity field is dynamically consistent with coherent rotation rather than with other features such as meanders or frontal intrusions, which have been documented in the central and marginal Arctic Ocean (e.g. von Appen et al., 2018; Von Appen et al., 2022; Zhao et al., 2014; Timmermans et al., 2008; Polyakov et al., 2012). As a first diagnostic, we require that the azimuthal (cross-track) velocity v_θ exhibit a reversal in sign across the centre of the isopycnal displacement, indicating opposite flow directions on the two flanks of the feature and ensuring that the profiler crossed through or very near the eddy core. As a second diagnostic, we test whether v_θ increases approximately linearly with radius within the core, consistent with the solid-body rotation expected in mesoscale eddies (Nurser and Bacon, 2014); the radius of maximum velocity then marks the edge of the core (Chelton et al., 2011). Because these dynamical diagnostics confirm coherent rotation, we also accept eddies sampled with fewer than the 4 ITP profiles required by Timmermans et al. (2008). In our dataset, the combined ITP–ADCP observations can confirm the presence of an eddy even when only two consecutive profiles show the isopycnal displacement.

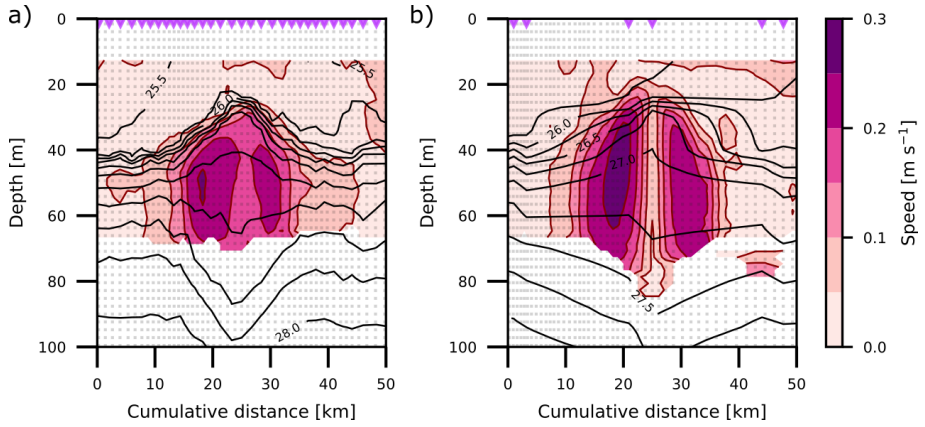

Figure 2. Cumulative distance–speed sections for (a) eddy E8 (January 15 2020) and (b) eddy E9 (February 12 2020). Black contours indicate isopycnals spaced every 0.25 kg m^{-3}. The dotted vertical light grey lines mark the ADCP measurement profiles, and the purple triangles mark the ITP measurement profiles.

To compute the cross-track component v_θ and its along-track counterpart v_r, the velocity profiles were rotated by the angle θ between consecutive drift-track segments:

$$v_r = u\cos(\theta) + v\sin(\theta) \tag{1}$$

$$v_\theta = -u\sin(\theta) + v\cos(\theta) \tag{2}$$

$$\theta = \arctan\left(\frac{y_2 - y_1}{x_2 - x_1}\right) \tag{3}$$

where (x_1, y_1) is the position of the first measurement and (x_2, y_2) of the second measurement. v_θ, also termed the swirl velocity, provides a sense of the rotation of the fluid (i.e., the tangential velocity component within a swirling flow).

In the theoretical Rankine vortex (Acheson, 1990), the azimuthal velocity increases linearly with the distance to the centre, having the maximum value of the velocity at $R_{\max}$; the distance between the location of the absolute smallest azimuthal velocity (centre of the eddy) and the maximum azimuthal velocity ($V_{\max}$) (Figure 3, red line). A method for computing the azimuthal velocity v_θ of a theoretical eddy as a function of radius (Equation 4) follows the analytical velocity model introduced initially by Castelão and Johns (2011), and later applied explicitly to eddy-velocity fitting by Castelão et al. (2013):

$$v_\theta(r) = \begin{cases} r\dfrac{V_{\max}}{R_{\max}}, & \text{for } r \le R_{\max} \\ V_{\max}\exp\left(-\dfrac{r - R_{\max}}{\lambda}\right), & \text{for } r > R_{\max} \end{cases} \tag{4}$$

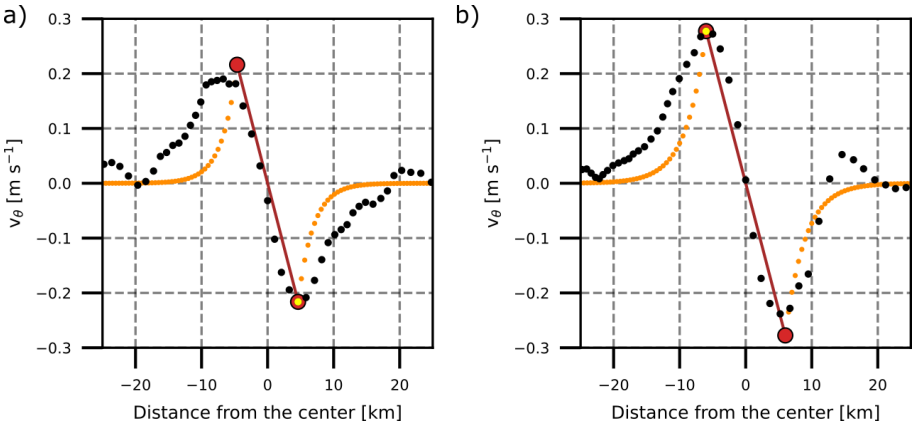

Figure 3. Azimuthal velocity (v_θ, ms^{-1}) for (a) eddy E8 (January 15 2020) and (b) eddy E9 (February 12 2020). Black dots show the measured $v\theta$ values at the depth level of maximum azimuthal velocity from ADCP data, computed using Equation 2. The solid red line represents the inner part of the Rankine vortex model (Equation 4, $r \leq R_{\max}$), while yellow dots represent the outer part (Equation 4, $r > R_{\max}$). The maximum azimuthal velocity ($V_{\max}$) used in the model is marked by a red dot with a yellow centre. The Rankine model is scaled using the maximum azimuthal velocity directly measured from the ADCP profiles (red dot with yellow centre).

where λ is a damping coefficient that indicates decay. Equation 4 assumes an inner part of the eddy that rotates like a solid body ($r \leq R_{\max}$) and an outer part ($r > R_{\max}$) where the velocity decays rapidly at the e folding scale λ, which is typically about $\frac{1}{3}\ R_{\max}$. Here, we are focusing on the inner part (i.e., the core of the eddy). Furthermore, the dynamics outside the limit of $R_{\max}$ are out of the scope of this study.

The azimuthal velocity (v_θ) calculated using Equation 2 was compared to the theoretical Rankine vortex (Equation 4) to assess whether the eddy cores exhibit solid-body rotation. In both E8 (January 15) and E9 (February 12) (Figure 3), the observed azimuthal velocity profiles measured by the ADCP closely follow the theoretical shape. The inner region displays solid-body rotation, while the outer region shows a rapid velocity decay, consistent with the Rankine vortex structure. For this comparison, the Rankine model is scaled using the maximum azimuthal velocity directly measured from the ADCP data along the drift trajectory, ensuring that the comparison reflects only the observations and the analytical model introduced in this subsection.

2.3 Determining the centre of the eddy and its radius

Several methods have been used to determine the centre of eddies in the open ocean. However, most need a surface expression of the eddy to obtain the horizontal velocity field (Chelton et al., 2011). In our study region, the presence of thick sea ice prevents the use of satellite-derived velocity fields, so the eddy centre must be inferred directly from the in situ ADCP observations. To estimate the centre of the eddy and obtain an accurate approximation of its radius, we applied the Maximum Swirl Velocity (MSV) method as described by Castelão et al. (2013). This method assumes that an eddy is axisymmetric, with all the momentum associated with the azimuthal component of the velocity. Hence, its centre is defined as the reference point

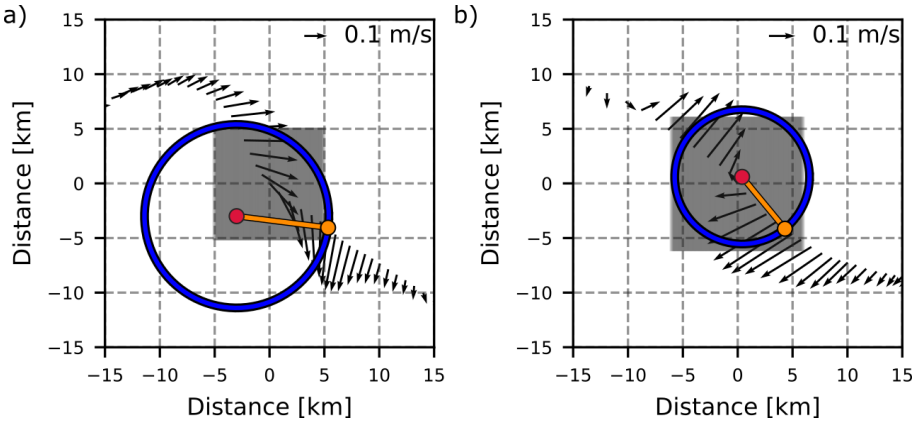

Figure 4. Velocity vectors of the eddies in (a) eddy E8 (January 15 2020) and (b) eddy E9 (February 12 2020) at the depth of maximum velocity. The grey area shows the grid used for the detection of the eddy centre, the red dot shows the estimated eddy centre using the methodology of Nencioli et al. (2008), the orange dot is the maximum azimuthal velocity (V_{max}) location and the orange line show the distance between the location of the absolute smallest azimuthal velocity (centre of the eddy) and V_{max}. The blue circle marks the inner part of the eddy. Equivalent plots for the remaining detected IHEs are shown in Appendix Figure A1.

in a cylindrical coordinate system that maximises the measured azimuthal velocity v_θ among the available data points, while the radial component of the velocity v_r is vanishing $V = \sqrt{v_\theta^2 + v_r^2} = v_\theta$.

To find the centre, we followed the approximation of Nencioli et al. (2008), who proposed testing the MSV method over a gridded search area, as follows. First, we defined an area of $2R_{max} \times 2R_{max}$ around the location where the minimum velocity inside the eddy was measured, dividing it into a 100 m resolution grid. We then used every point of the grid as a theoretical centre, decomposing all of the ADCP velocities, as in Equation 1-3, into tangential and radial components relative to each candidate centre. As v_θ has opposite signs for cyclones and anticyclones, it is easier to determine the centre of the eddy by finding the location where v_r is minimal, thereby minimising the cost function J (Castelão et al., 2013):

$$J = \frac{1}{2N} \sum_{n=1}^{N} \left(\frac{v_{rn}}{V_n} \right)^2 \tag{5}$$

where N is the number of ADCP measurements used and V is the speed. To perform this minimisation, we computed the value of J at every grid point and selected as the eddy centre the point where J reached its minimum. Once the centre is detected, we recalculated the radius R_m as the distance between the theoretical centre and V_{max} (as shown in Figure 4).

We apply this eddy detection method to eddies E8 and E9 (Figure 4). The centre of the eddy E8, calculated by minimising the cost function J, lies approximately 5 km from the point of minimum velocity in the transect, and its radius is estimated at 8.4 km. In contrast, the radius obtained by measuring the distance between the locations of minimum and maximum velocity along the same transect is considerably smaller, about 4.6 km. For eddy E9, the L2 transect crossed nearly through its centre, and the difference between the two radius estimates is minimal (5.9 km - 6.1 km).

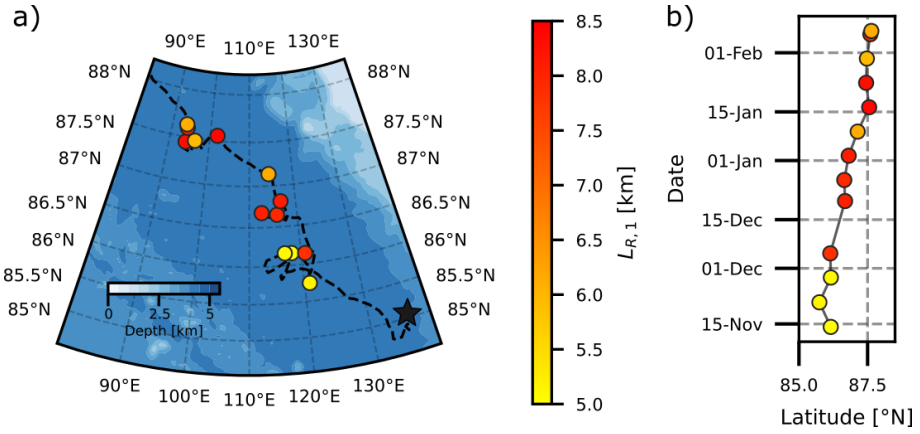

Figure 5. The first baroclinic Rossby radius of deformation mode ($L_{R,1}$) calculated from CTD vertical casts obtained aboard *Polarstern* during the MOSAiC drift (dashed black line), with the start of the drift (19 October 2019) marked by a black star. Spatial distribution of $L_{R,1}$ is shown in (a), and the time series of $L_{R,1}$ as a function of latitude is shown in (b).

2.4 Calculation of Rossby radius

The Rossby radius of deformation is a fundamental scale in geophysical fluid dynamics that characterises the horizontal extent over which baroclinic processes, such as eddies, are influenced by the Earth's rotation. It represents the length scale at which the restoring force due to stratification (buoyancy) is balanced by the Coriolis force (rotation), and is thus a critical parameter in controlling the dynamics of mesoscale structures (Nurser and Bacon, 2014). To constrain the local scale of these mesoscale processes, we calculated the first mode of the baroclinic Rossby radius of deformation using the approximation of Wang et al. (2013) (Equation 6):

$$\frac{\partial}{\partial z}\left(\frac{f^2}{N^2}\frac{\partial F_m}{\partial z}\right) = -\frac{1}{L_{R,m}^2}F_m, \tag{6}$$

where N, the Brunt–Väisälä frequency, is derived from the CTD vertical cast. f is the Coriolis parameter ($f = 1.45 \times 10^{-4} s^{-1}$), F_m is the dynamic mode eigenfunction and $L_{R,m}$ is the Rossby radius of the m^{th} baroclinic mode. To solve this equation, we apply a flat-bottom boundary condition ($\frac{dF_m}{dz} = 0$ at $z = 0, -H$), appropriate for our study region within the deep Amundsen Basin. Although the Amundsen Basin is limited by the Lomonosov and Gakkel Ridges, our study area lies in the central interior of the basin, where the upper-ocean stratification and water-mass structure are known to be horizontally uniform and largely independent of ridge-controlled dynamics (Rudels et al., 1996)

In Figure 5, we show the spatial distribution of $L_{R,1}$ in our study area. Stations located close to each other sometimes show different $L_{R,1}$ values, likely due to local variations in the vertical stratification of the water column. These differences reflect the sensitivity of the method to small-scale changes in water column stability, which are captured in the CTD profiles. The

mean value of $L_{R,1}$ in the study area is 6.93 km, which justifies our use of the term (sub)mesoscale throughout the paper, as several eddy structures observed fall near or below this threshold.

3 Results

3.1 Examples of two characteristic eddies

We observed nine eddies, which, for the purpose of explanation, we label E1 to E9. We start this section by analysing in detail two representative anticyclonic eddies: E8, observed on January 15, and E9, observed on February 12 (see Tables 2)-3. These examples are used throughout the Methods section to illustrate our detection and characterisation approach. The E8 eddy (Figure 6-7, upper panels) was captured by the L3 buoys with 12 ITP profiles and 10 ADCP profiles within the solid-body rotation region (core). The MSV method (see section 2.3) revealed a radius of 8.4 km. The E9 eddy (Figure 6-7, lower panels), captured by the L2 buoy with only 2 ITP profiles and 9 ADCP profiles, had a radius of 6.14 km. We selected these two eddies because they were the largest and most energetic detected along the drift track, with strong azimuthal velocities and clear hydrographic signatures representative of wintertime IHEs. Although the CTD profiles only coarsely resolved E9, the ADCP data did resolve it well, and it suggests the eddy was crossed almost through its centre (Figure 4).

To characterise the eddies, we used profiles of conservative temperature (Θ), absolute salinity (S_{A_C}), density (σ_θ), buoyancy frequency (N), and azimuthal velocity (v_θ) (Figure 7). We selected the central profile, where the isopycnal displacement was greatest, based on ITP data (Figure 6a-b, red dashed line). The N profiles were used to identify the isopycnal surfaces that bound each eddy vertically. We define the upper limit of the eddy (Figure 6-7, red line) as the isopycnal coincident with the depth of the first peak in N, and the lower limit (Figure 6-7, cyan line) as the isopycnal coincident with the depth of the second peak in N, and the core-centre is defined as the depth where N reaches a minimum between these two limits. Our definition of the core-centre depth differs from that used by Timmermans et al. (2008), who used the level of minimum Θ. That criterion was not applicable to the eddies observed in this study, as no clear Θ minimum was present. The eddy thickness is thus given by the depth difference between its upper and lower boundaries. The eddies observed are IHEs, located near the base of the mixed layer and interacting with the upper halocline. As they translate, they uplift the mixed layer, making it thinner. The eddy E8 yielded a decrease in the MLD from 41 m to 24 m from the eddy edge to the eddy centre, which is similar to that resulting from the eddy E9, with a decrease of 20 m depth. At the upper boundary, the isopycnal was displaced upwards 14 m in both eddies; at the lower boundary, it was displaced downwards by 23 m in E8 and 19 m in E9. In E8, the eddy's upper boundary is located at depth with $v_\theta \approx 0$ (Figure 7d), indicating good agreement between the CTD and ADCP data. In E9, the eddy's upper boundary, as determined using the N profiles, does not align with the depth with $v_\theta \approx 0$, likely due to the coarser temporal resolution of the CTD data. The maximum azimuthal velocity of the eddy was 0.25 ms^{-1} and 0.28 ms^{-1} in E8 and E9, respectively.

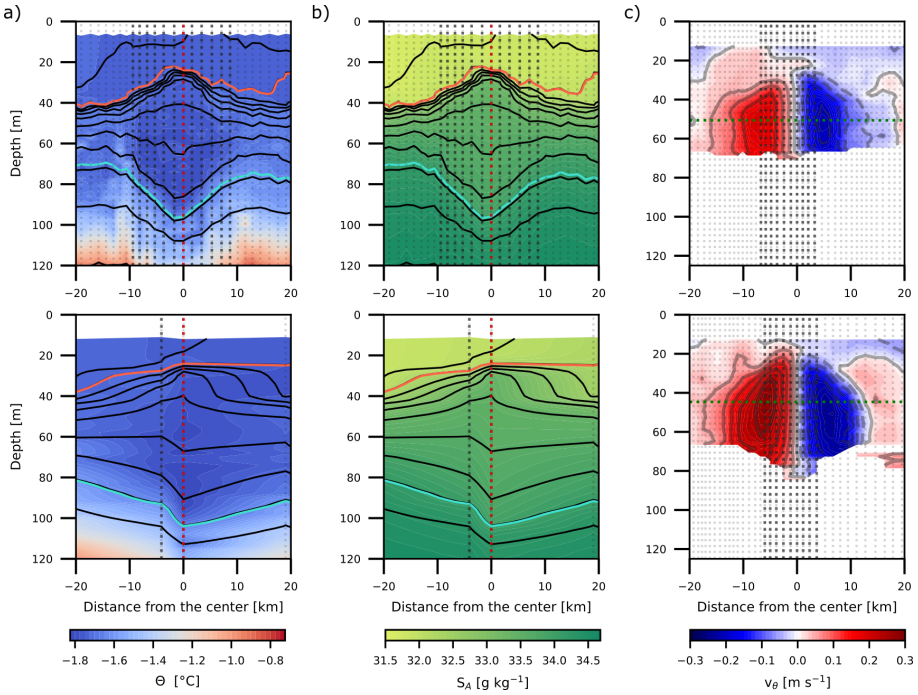

Figure 6. Details of the eddies E8 (upper panel) and E9 (lower panel). (a) Cross sections of conservative temperature (Θ) and (b) absolute salinity (g kg^{-1}) with isopycnals shown as black contours spaced every 0.25 kg m^{-3}; red and cyan contours indicate the upper and lower limits of the eddies, respectively, and the dashed vertical red line marks the central eddy profile. (f) Cross section of azimuthal velocity v_θ with velocity contours in grey every 0.05 ms^{-1}. The green dotted line indicates the depth of maximum velocity. The dotted vertical light grey lines in (a), (b) and (f) marker the measurement profiles, where the darker lines are the profiles inside the eddy in Figure 7. Equivalent plots for the remaining detected IHEs are shown in Appendix Figure A2-A3.

3.2 Properties of all eddies detected during the winter season

In the period from October 19 2019 to March 15 2020, we detected nine well-developed anticyclonic eddies in the central part of the Amundsen Basin (Figure 8a, Tables 2-3). These eddies are consistent with our criteria, showing evident isopycnal displacement and solid-body rotation. At the L3 site, we sampled five eddies at high horizontal resolution, enabled by the high-frequency sampling of both ITP and ADCP instruments at this location (Figure 8, diamond markers), and their presence is evident in both the isopycnal displacement and the large subsurface azimuthal velocity. The ITP at the L2 site had a more complex profiling schedule (Table 1), with a greater horizontal distance between consecutive profiles, making the identification of eddies by isopycnal displacement alone more challenging. However, when analysing the ADCP data, we detected one eddy in December and one in February (Figure 8, square markers). We do not have hydrographic data for the inner part of the eddy in December (E7), and only two profiles are available for the eddy in February (E9). At the L1 site, we detected two eddies, one in October (E3) and one in November (E4) (Figure 8, inverted triangle markers). There is a one-month gap in eddy detections

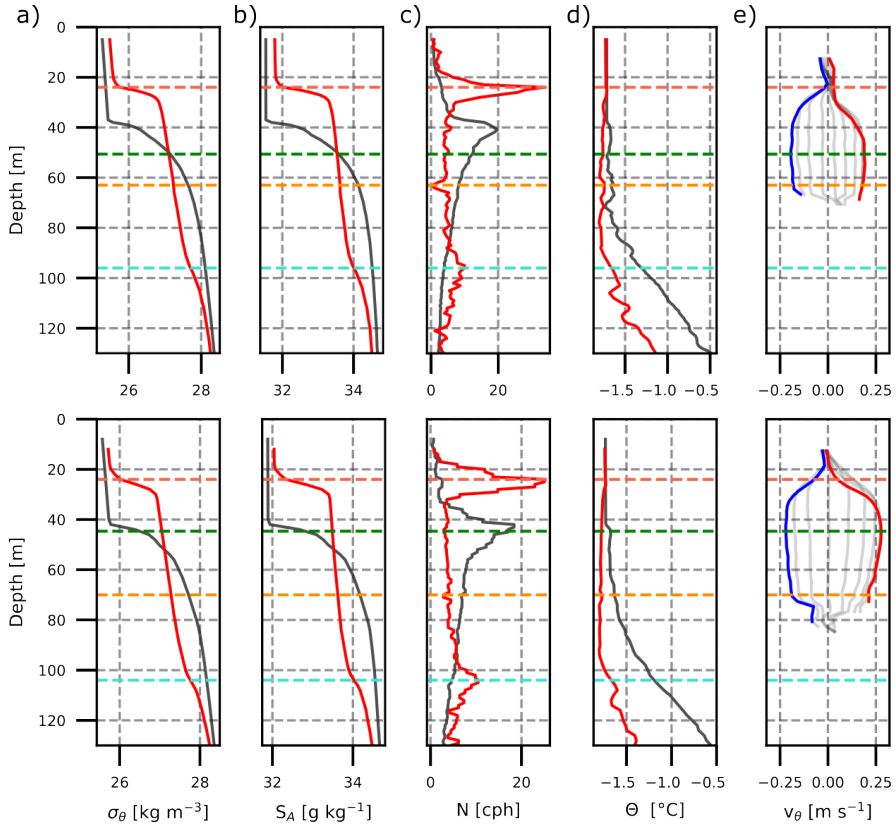

Figure 7. Details of the eddies E8 (upper panel) and E9 (lower panel). Vertical profiles of density (σ_θ) (a), absolute salinity (g kg^{-1}) (b), buoyancy frequency (N) (c), conservative temperature (Θ)(d), and azimuthal velocity (v_θ) (e). The red line shows the central profile, and the grey line shows the mean profiles at $\pm$ 20 km around the eddy, marked as dotted vertical light grey lines in Figure 6. Dashed horizontal lines show the top (red), the bottom (cyan), the maximum azimuthal velocity level (green) and the eddy core-centre depth (orange). Equivalent plots for the remaining detected IHEs are shown in Appendix Figure A4-A5.

in the DN (December 17, 2019 – January 15, 2020). However, there were no obvious changes in the drift speed of the DN during that period (Figure 1c, mean speed of $\sim$0.1 ms^{-1}). Hence, the absence of eddies is likely unrelated to the temporal and spatial resolution of the measurements.

We now describe the mean properties of the detected eddies (Figure 8 and Tables 2-3). The dynamical nature of the eddies can be characterised through the interplay between four key parameters: the eddy radii estimated from the MSV (R_m = 6.09 $\pm$ 1.4 km), the first mode of the baroclinic Rossby radius of deformation ($L_{R,1}$ = 6.9 $\pm$ 1.3 km), the maximum azimuthal velocity (V_{max} = 0.14 $\pm$ 0.07 ms^{-1}), and the Rossby number (R_o = 0.32 $\pm$ 0.14). The condition $R_m < L_{R,1}$ places these eddies in the (sub)mesoscale regime, indicating a transitional dynamical scale. Consistent with this interpretation, the Burger number (Bu) computed for the nine eddies (0.4–2.9) further show that most lie in a submesoscale-to-mesoscale transitional regime ($Bu \approx 1$), while a minority ($Bu > 1$) exhibit more compact structures where cyclogeostrophic effects may become relevant. We computed

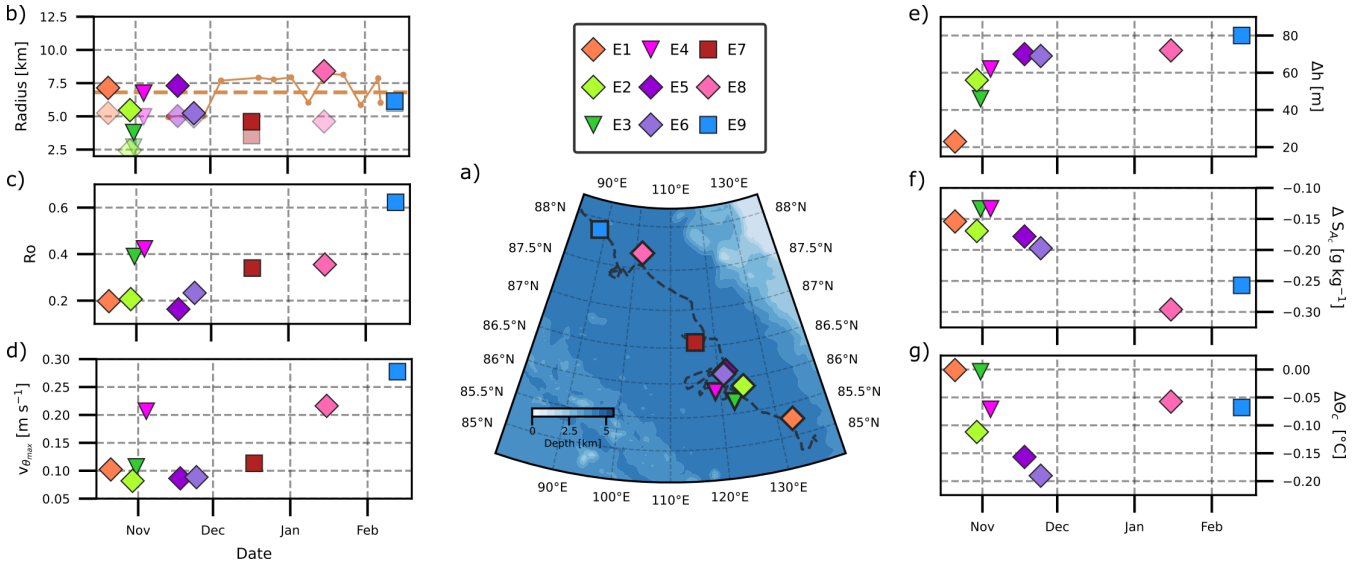

Figure 8. Properties of the nine eddies (E1–E9) detected during the winter 2019–2020 MOSAiC drift and their spatial locations (a). Markers indicate the L-site of detection (inverted triangles: L1, squares: L2, diamonds: L3). Time series panels show the eddy radius (b), Rossby number (Ro) (c) and maximum azimuthal velocity ($V_{\theta_{max}}$) (d) on the left; and eddy thickness (Δh) (e), core-centre absolute salinity anomaly (ΔS_{A_C}) (f) and core-centre conservative temperature anomaly ($\Delta\Theta_C$) (g) on the right. In (b), we compare the radius estimated from the distance between $V_{\theta_{max}}$ and the centre located in the buoy drift (Figure 3, translucent markers) with that calculated using the MSV method (Figure 4). The first mode of the Rossby radius $L_{R,1}$ is shown in orange, with mean values indicated by dashed lines in the same colour.

R_o using the cylindrical approximation $Ro = \frac{2U}{fR}$ (Zhao et al., 2014), where U is V_{max}, f is the Coriolis parameter and R is the radius. Similarly, the Burger number was computed as $Bu = (\frac{R}{L_{R,1}})^2$, where $L_{R,1}$ is the first baroclinic Rossby deformation radius. This yields R_o ($0.16 < R_o < 0.62$) that is consistent with the quasi-geostrophic balance, although the upper range allows for curvature effects (e.g., Shakespeare, 2016). It is interesting that the radii would be underestimated by ≈ 1.7 km if we did not perform the MSV correction (Figure 8b), which would indicate that the eddies appear closer to the submesoscale regime than they actually are. In the centre of the eddies, the MLD becomes shallower on average by 11.5 ± 5.73 m, ranging from 33.6 to 22.12 m depth. The eddy thickness differs by 23 to 80 m, having an average thickness of 59.75 ± 18.1 m. The depth of the eddy centre (D_c) were found at 59.3 ± 13.6 m depth with an average temperature of Θ_c =-1.773 ± 0.04°C, salinity of S_{A_c} =33.954 ± 0.26 and a potential density of σ_{θ_c} =27.49 ± 0.24 kg m^{-3}. These values correspond to the range of surface waters in the Amundsen Basin, but then, if we look at the anomalies against the mean values of the profiles at $\pm$ 30 km around the eddy, we find small yet significant anomalies ($\Delta\Theta_c$ = -0.082°C, ΔS_{A_c} = -0.189 g kg^{-1}, $\Delta\sigma_{\theta_c}$ = -0.15 kg m^{-3}), that we will use later to discuss the possible origin of the eddies.

In the Arctic Ocean, density is primarily driven by salinity changes (Figure 6b and 7b) rather than temperature due to the well-developed halocline, as cold waters remain close to the freezing point, minimising thermal effects (Aagaard and Carmack, 1989; Carmack et al., 2016). This dependency is evident in the core-centre properties, with density anomalies linearly

Table 2. Summary of hydrographical properties of all detected IHEs during the winter MOSAiC drift. Eddies are labelled sequentially (E1 to E10) based on their chronological order of detection. Mixed layer depth in the central profile/mean water state ΔMLD [m], thickness Δh [m], core-centre depth D_c [m], core-centre values of conservative temperature Θ_c [°C], absolute salinity S_{A_c} [g kg^{-1}], density σ_{θ_c} [kg m^{-3}], their anomaly values, and number of ITP and ADCP profiles within the eddy core.

Eddy	Site	Date	ΔMLD	Δh	D_c	Θ_c	S_{A_c}	σ_{θ_c}	$\Delta\Theta_c$	ΔS_{A_c}	$\Delta\sigma_{\theta_c}$	ITP-ADCP profiles
E1	L3	21–10	22/31	23	36	-1.72	33.84	27.28	-0.001	-0.154	-0.124	8–6
E2	L3	29–10	19/29	56	73	-1.71	34.26	27.80	-0.111	-0.169	-0.133	15–8
E3	L1	31–10	28/32	46	54	-1.78	34.09	27.57	-0.003	-0.133	-0.107	2–6
E4	L1	04–11	16/35	62	43	-1.80	33.81	27.29	-0.071	-0.133	-0.105	4–8
E5	L3	17–11	23/29	70	69	-1.81	34.18	27.72	-0.156	-0.178	-0.139	4–4
E6	L3	24–11	21/30	69	67	-1.83	34.19	27.72	-0.190	-0.197	-0.153	8–6
E7	L2	17–12	–	–	–	–	–	–	–	–	–	0–9
E8	L3	15–01	24/41	72	63	-1.74	33.62	27.23	-0.057	-0.296	-0.237	12–10
E9	L2	12–02	24/42	80	70	-1.77	33.63	27.27	-0.067	-0.257	-0.205	2–9

Table 3. Summary of dynamical properties of all detected IHEs. Eddy radius R_m [km], maximum azimuthal velocity V_{max} [m s^{-1}], depth of maximum velocity D_{V_m} [m], Rossby number Ro, and Burger number Bu.

Eddy	R_m	V_{max}	D_{V_m}	Ro	Bu
E1	7.14	0.10	33	0.19	0.4
E2	5.46	0.08	33	0.20	0.8
E3	3.78	0.10	45	0.38	1.7
E4	6.74	0.20	37	0.42	0.5
E5	7.30	0.08	65	0.16	0.4
E6	5.23	0.08	63	0.23	0.9
E7	4.59	0.11	47	0.34	2.9
E8	8.40	0.21	49	0.35	0.9
E9	6.14	0.27	45	0.62	0.9

associated with salinity anomalies (Figure 9a). However, the relationship between V_{max} and the eddy thickness does not follow a single linear trend (Figure 9c), where we can distinguish two different groups. The first one with lower V_{max} and Rossby numbers $Ro \approx 0.2$, where the relative vorticity term ($2V_\theta/r$) represents only about 20% of the planetary vorticity (f), and the second group with lower $Ro(\approx 0.3$–$0.6)$, where relative vorticity accounts for 30–60% of f. This separation in Ro is consistent with the natural segmentation apparent in the Ro distribution itself (Figure 9b), which qualitatively corresponds to what a

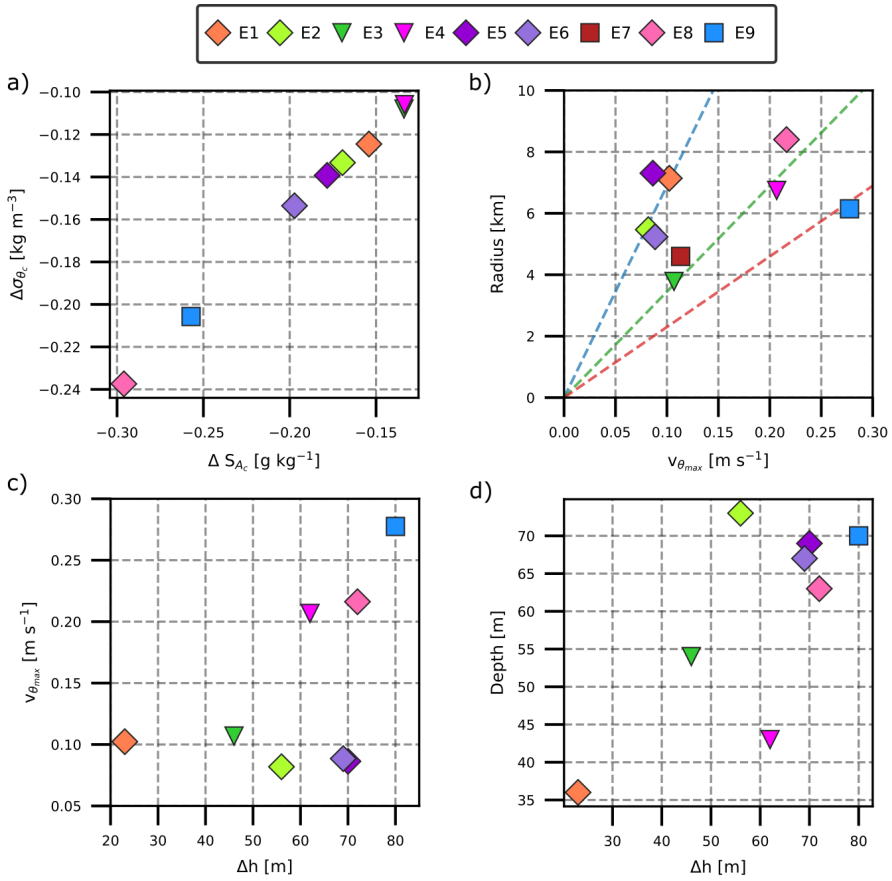

Figure 9. Scatter plots of: a) density anomaly ($\Delta\sigma_{\theta_c}$) versus salinity anomaly (ΔS_{A_c}), b) Radius versus maximum azimuthal velocity (V_{max}) with dash lines showing Ro of 0.2 (blue), 0.4 (green), and 0.6 (red), c) maximum azimuthal velocity (V_{max}) versus thickness (Δh) and d) Core-centre depth (D_c) versus thickness (Δh).

non-parametric clustering approach would identify. Higher Ro eddies require stronger velocity adjustments to balance changes in thickness, and for these cases, the Coriolis force alone becomes insufficient to balance the radial pressure gradient. The centrifugal contribution therefore becomes relevant, indicating that those eddies are closer to the cyclogeostrophic regime in which both Coriolis and centrifugal forces balance the pressure gradient, consistent with the findings of Zhao et al. (2014). In contrast, low Ro eddies can accommodate thickness variations with comparatively small changes in V_{max}, reflecting different modes of potential vorticity adjustment (Cushman-Roisin and Beckers, 2011). This behaviour is also consistent with their thermohaline structure: the more energetic eddies not only tend to be thicker, but also exhibit larger core-centre anomalies. We find that most of the eddies with larger thickness are located deeper in the water column (Figure 9d).

No eddies were detected after February 12, the date of the last confirmed detection. Although the DN continued drifting, the velocity measurements became progressively limited due to the sequential failure of the AOFBs, first at L1 (February

27) and later at the Central Observatory (March 19), leaving the sADCP as the only velocity source, which did not reveal any coherent eddy signatures. Meanwhile, the ITPs at L1 and L2 remained operational but did not register additional eddies. By mid-March, after the drift crossed the Gakkel Ridge and transitioned to the Nansen Basin, the mixed layer had deepened markedly (exceeding 150 m), which likely inhibited the detection of IHEs within the 200 m vertical range of the remaining ITPs.

4 Discussion

4.1 Detection of duplicate eddies

The study of eddies under sea ice prompts the question of whether the same eddy has been sampled several times. The answer to this question is not trivial; all the different measurements need to be assessed to constrain it. First, the assumption of quasi-synoptic conditions adopted in section 2.2 implies that the eddies cannot move fast enough to pass several sites within the time frame of a single observation period. Second, the eddy size provides an additional constraint: most IHEs observed by Zhao et al. (2014) in the Amundsen Basin had radii of approximately 5 km, consistent with our estimates. Given the spatial separation among the DN sites, L1–L3 $\approx$ 32–35 km, L1–CO $\approx$ 10–17 km, and L3–CO $\approx$ 22–24 km, it is therefore unlikely that the same eddy would be sampled at more than one location, except in the few cases where the drift geometry brought two platforms over the same region within a short time interval. Third, the mean background flow of the Transpolar Drift, about 0.02 $\mathrm{m\,s^{-1}}$, advects the IHEs at approximately the same speed (Zhao et al., 2014), further limiting the distance an eddy can travel between consecutive profiles. Although the DN rotated during the drift, its overall configuration and relative distances remained effectively constant throughout the study period (Figure 1b). Therefore, rotation does not alter the spatial separation between sites nor create conditions under which a single eddy could be sampled simultaneously at different locations. In the specific cases of E7 and E9, the CO ADCP detected an eddy shortly before the L2 ITP sampled a similar signal. Because the DN drifted northeastward–southeastward, both platforms consecutively passed over the same region, separated by approximately 9–14 km, allowing us to conclude that L2 and CO sampled the same eddy. These are the only two eddies detected at L2, and since L2 does not provide velocity measurements, such events represent the only situations in which L2 can be meaningfully compared with CO. Moreover, during the periods when E7 and E9 were observed, no eddy signatures were detected at L1 or L3, further limiting the usefulness of L2 for the multi-site duplicate-detection analysis presented below. We therefore examine possible duplicate detections only for the configurations in which velocity and hydrographic data allow meaningful cross-comparison.

Between October 29 and November 29, 2019, five eddies were observed at different L sites within a relatively short time window, raising the possibility that some of these detections correspond to the same eddy sampled at various stages of its path. Although the distances between sites such as L1 and L3 exceed 30 km—well beyond the radius of the eddies in the area of $\sim$6 km—, the temporal coincidence warrants a closer investigation into whether some of these eddies could have drifted between nearby sites, particularly those closer together such as L2 and CO. For instance, L1 and L3 detected an eddy within two days (E3 on October 31 and E2 on October 29; Figure 10, panels c and a, green and lime circles). Both events fall within the smaller-radius range but exhibit different core characteristics. The sADCP from *Polarstern* (Figure 10b, right panel) shows

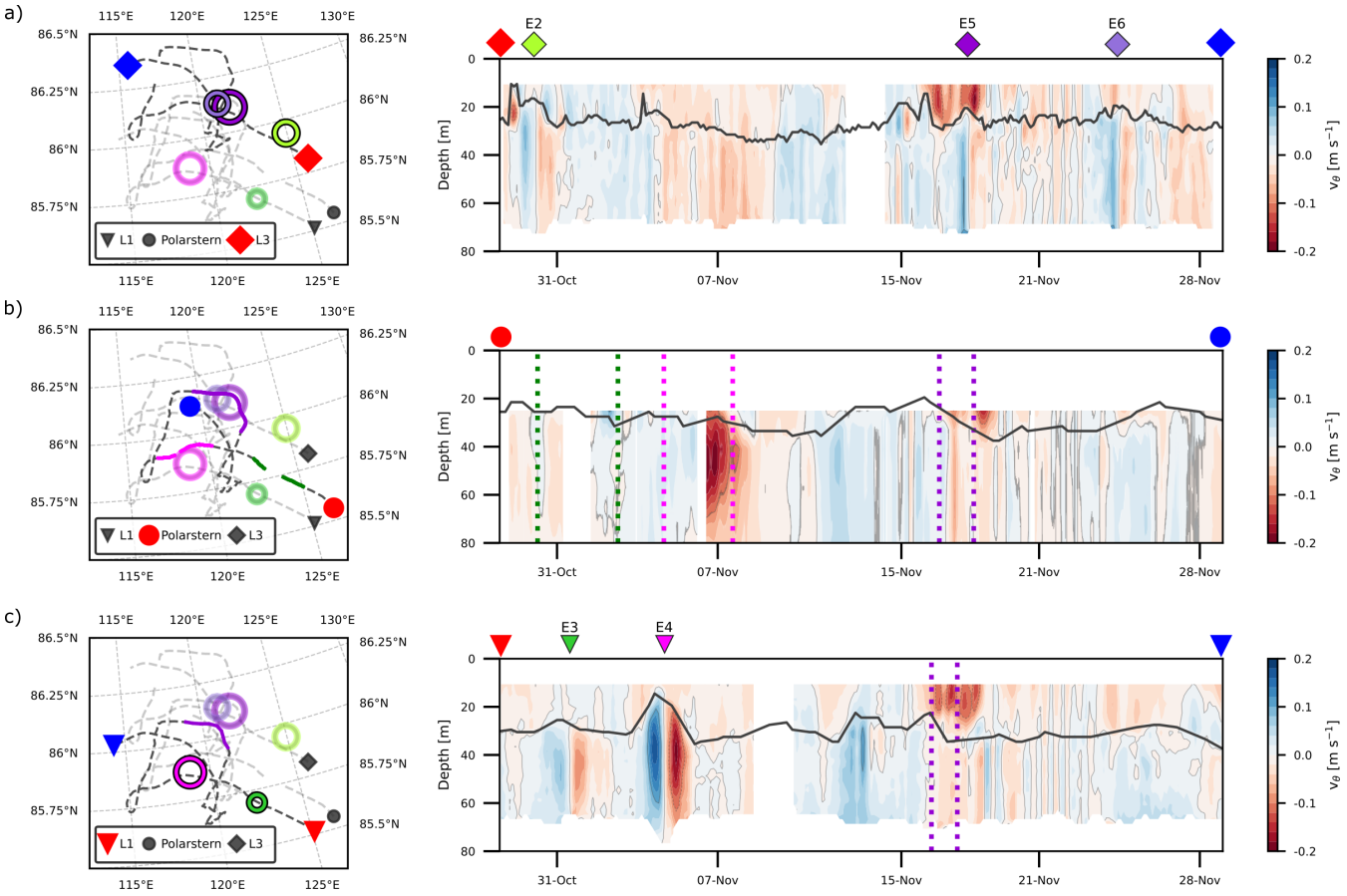

Figure 10. Drift pathways and cross-track velocity sections for the L-sites from October 29 to November 29. Panels (a), (b), and (c) correspond to sites L3, CO (Polarstern), and L1, respectively. Each panel includes a map on the left showing the drift trajectory of the corresponding site (in dark grey), with the starting point marked by a red symbol and the endpoint by a blue one. The trajectories of the other two sites are shown in light grey for reference. Eddy locations are represented as coloured circles, scaled by their estimated radius and matching the colours used in the left panels. Circles are shown in full colour when the eddy was sampled by the site, and translucent otherwise. The right-hand panels display the cross-track velocity along each site's drift path. Eddies whose cores were crossed are marked with symbols at the top of the panels. When a site passed near the location of a previously detected eddy, this is indicated by a solid-colour segment along the drift path (left panel) and by dashed vertical lines of the same colour in the velocity section (right panel).

no velocity signature associated with either eddy during the period marked by the green dashed line. Therefore, the two eddies appear dynamically independent, and the CO site did not intersect the azimuthal circulation of either feature during its drift. From November 15 to 19, a storm affected the ice drift, increasing the speed up to 0.4 ms^{-1} (Figure 1c) and changing the drifting direction several times (Figure 10, left panels). As a result, the DN platform sampled some sites more than once. Of
335 the three eddies encountered on November 4 (E4), 17 (E5), and 24 (E6) (Figure 10, pink, lilac and purple circles), E4 stands out as a well-formed eddy with a strong azimuthal velocity of V_{max} = 0.20 ms^{-1} (Figure 10c, right panel). The periphery of

this eddy was also observed at the CO site on November 7 (Figure 10b, right panel, dashed pink line), as confirmed by the drift trajectory of CO passing near the core's edge. Site L3 recorded two eddies within a week, with centres separated by 6 km. This suggests that both detections correspond to the same eddy, which would have a translation speed of approximately 0.01 $\mathrm{m\ s^{-1}}$ during that period. The thermohaline and kinematic properties support this interpretation (Tables 2-3): the differences between E5 and E6 are minimal (order 0.01 in Θ and S_A) and are consistent with the instruments not sampling the same cross-section of the eddy, which also explains the moderate difference in estimated radius (7.3–5.2 km). The Θ-S_A structure (Figure 12c) confirms that both features share nearly identical core water masses, indicating no appreciable modification of the eddy over the one-week interval. This is expected, as intrahalocline eddies can persist for extended periods. Zhao et al. (2014) report a lifespan of at least 21 months for Eurasian Basin IHEs, and therefore their thermohaline structure is not expected to change substantially on weekly timescales. Although the CO site passed near the region where the eddy was located, no clear azimuthal-velocity anomaly was detected (Figure 10b, purple line), likely due to an earlier partial crossing or an incomplete intersection with the eddy core.

4.2 Origin and generation of eddies

Unlike temperate seas, the generation and trajectory of eddies cannot be remotely observed beneath Arctic sea ice. Although the western Nansen Basin shows stronger eddy kinetic energy than the interior Eurasian Basin, weaker and less frequent eddies have also been observed in the central Arctic (Von Appen et al., 2022). Literature shows that most of the efforts to categorise Arctic eddies have focused on the differences in the thermohaline properties of their cores. Based on this, eddies have been classified into Canadian water and Eurasian water eddies. In turn, this classification is divided into shallow (<80 m) and mid-depth (>80 m) core-centre depth, respectively (e.g., Zhao et al., 2014). The eight eddies found in this study are shallow Eurasian water eddies, containing saltier waters that are less close to the freezing point than those studied by Zhao et al. and therefore depart from the temperature–salinity relationship reported in that study (Figure 11b).

The Θ-S_A diagram in Figure 12 shows three different characteristic shapes: (i) fluctuant temperature with a smooth "wedge" shape in E8 and E9 (Figure 12a) located approximately within the range of $-1.74 \pm 0.03°\mathrm{C}$ and $33.62 \pm 0.1\ \mathrm{g\ kg^{-1}}$, (ii) a smoother curve in October (Figure 12b) and (iii) a prominent "wedge" shape in November (Figure 12c) around $-1.81 \pm 2°\mathrm{C}$ and $34 \pm 0.3\ \mathrm{g\ kg^{-1}}$. By "wedge shape," we refer to a T–S structure in which temperature decreases toward a local minimum at the eddy core-centre, and then increases again as salinity continues to rise, forming a characteristic concave shape in the diagram. The smooth curve in Figure 12b is the typical Θ-S_A diagram observed in the surface Amundsen Basin water, with the temperature minimum just above the thermocline (Rudels et al., 1996). It results from advective-convective processes (Steele and Boyd, 1998). Following the formation of the winter mixed layer, fresher water originating from the Russian shelves and transported via the Transpolar Drift reaches the freezing point and becomes dense enough to convectively mix with the existing mixed layer (Kikuchi et al., 2004). This process generates the cold halocline layer, a key feature of the Nansen Basin surface structure. In summer, meltwater from sea ice accumulates at the surface, stratifying above the cold halocline layer. As freezing resumes in early winter, this freshwater cools to the freezing point and begins to convect into the halocline, forming the distinctive Θ–S_A "wedge" shape.

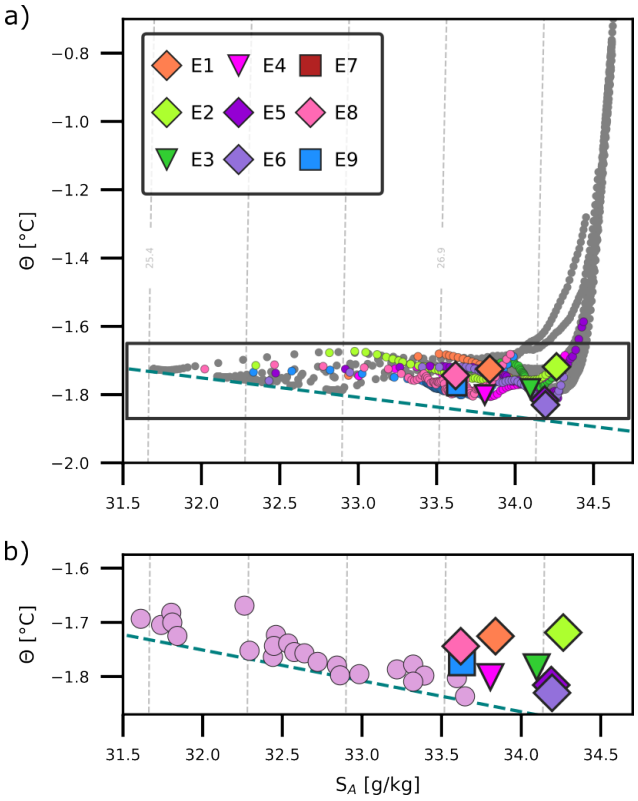

Figure 11. Θ-S_A diagrams. Density contours and freezing temperature (at surface pressure) are shown in grey dashed lines and in blue dashed lines, respectively. Mean profiles of the surrounding water are shown in grey, and the colours represent each eddy up to 90 meters depth with the core-centre properties shown by the larger markers. b) shows the core-centre Θ-S_A values, and in pink the core-centre values of Eurasian eddies from Zhao et al. (2014).

Figure 12c shows the Θ-S_A diagram arising from a convective cold halocline, resulting from the stratification of summer sea ice meltwater and the remnants of a winter mixed layer (Steele and Boyd, 1998). It has the particularity of a prominent wedge, typical of surface conditions in the Nansen Basin during late autumn, when the water column is actively adjusting to the changing surface freshwater input and atmospheric cooling. A similar process occurred inside the eddy (Figure 12a), but
375 the refreezing and convection during winter altered the upper part, making the wedge smoother than in the early winter season (Kikuchi et al., 2004). Comparing the Θ-S_A diagram of the eddies with the surrounding water, we find that E1 and E2 have trapped similar water masses, suggesting these eddies were likely formed in the same region. The Θ-S_A diagrams of the other eddies have a wedge shape consistent with the typical processes occurring at the surface of the Nansen Basin, which is not seen in the surrounding waters at the time of the observations.

380 Water mass analyses provide valuable insight into the stratification and convective processes that likely precondition the upper ocean before eddy formation and may help infer their possible region of origin. In particular, the presence of cold,

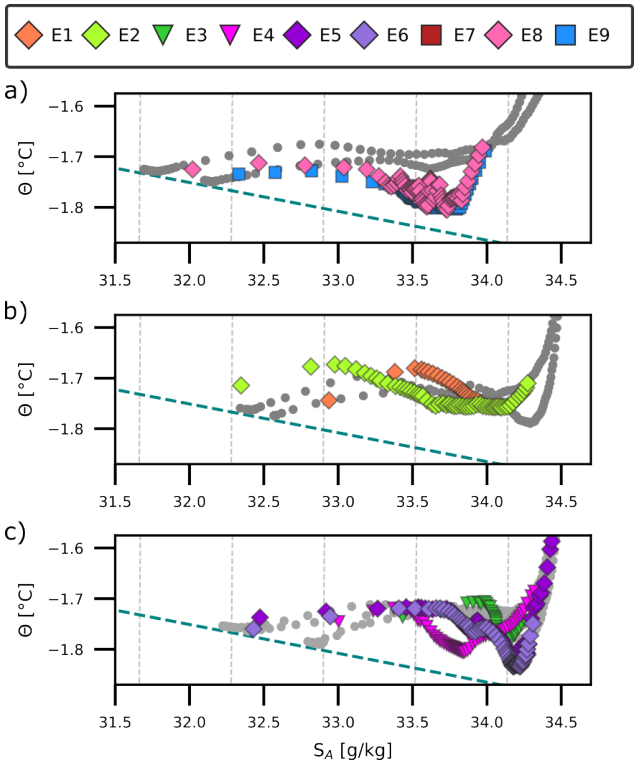

Figure 12. Θ-S_A diagrams. Density contours and freezing temperature (at surface pressure) are shown in grey dashed lines and in blue dashed lines, respectively. Mean profiles of the surrounding water are shown in grey, and the colours represent each eddy up to 90 meters depth with the core-centre properties shown by the larger markers. Groups of eddies with similar Θ-S_A curves indicating different generation processes: a) refreezing and convection, b) advective-convective and c) convective cold halocline.

fresh anomalies and a sharpened halocline in the eddy cores suggests that local convection during winter, possibly associated with lead refreezing, played a role. Additionally, the geographic location of the eddies—well within the Transpolar Drift path—indicates that they may have formed upstream, in regions influenced by freshwater input from the Siberian shelves. This supports the hypothesis that baroclinic instability, facilitated by strong vertical stratification and preconditioning from prior surface forcing (e.g., convection in leads), is a plausible generation mechanism (Bush and Woods, 2000). Another hypothesis, supported by observations and modelling, suggests that baroclinic instabilities—largely independent from surface conditions due to the persistent stratification—could be the dominant generation mechanism throughout the year (Meneghello et al., 2021). Comparable generation pathways have been documented elsewhere in the Arctic, where jets flowing along topographic gradients or strong shelf–basin density fronts trigger instabilities that form subsurface eddies and intermediate layers (MacKinnon et al., 2021; Schulz et al., 2021). Although the central Amundsen Basin lacks the intense boundary-current jets present near the Siberian margin, these studies illustrate how localised shear and preconditioning can seed baroclinic instabilities in strongly stratified Arctic environments, and would favour the hypothesis that some of the eddies we observed formed in the basin near

the Siberian continental slope. These mechanisms are not mutually exclusive: thermohaline convection in leads may precondition the water column, creating vertical shear and density structures that enable baroclinic instability. Thus, eddy generation may result from a combination of surface-driven convection and deeper baroclinic adjustment, even in the basin interior.

5 Conclusions

This study presents a detailed characterisation of intrahalocline eddies (IHEs) in the Amundsen Basin, based on hydrographic and velocity data collected during wintertime in the MOSAiC expedition. Nine well-defined anticyclonic eddies were identified, corresponding to eight distinct intrahalocline eddies, one of which was sampled twice, with radii of R_m = 6.09 $\pm$ 1.4 km and thicknesses ranging from 23 to 80 m, all exhibiting solid-body rotation. The thermohaline properties of the water masses trapped within their cores allowed us to infer pre-existing stratification conditions, providing insight into the environmental background from which these eddies formed.

Our results show that IHEs locally alter the vertical stratification, shoaling the mixed layer by over 10 m and affecting the stability of the halocline. Their horizontal and vertical scales, together with Rossby numbers in the range 0.16 < R_o < 0.62, place them within a transitional dynamic regime between meso- and submesoscale, consistent with quasi-geostrophic dynamics. Applying the Maximum Swirl Velocity (MSV) method resulted in radius estimates that were on average 1.7 km (25%) larger than those obtained using simpler transect-based methods. This correction is relevant because underestimating eddy size can lead to significant misinterpretation of their transport capacity, energy content, and dynamical role, particularly in under-ice conditions where spatial sampling is sparse.

The consistent presence of cold and fresh anomalies in the eddy cores suggests that local convection and/or baroclinic instability may play a role in their formation. Future studies would benefit from higher-resolution (2–3 km) spatially distributed autonomous observations capable of resolving the typical 6 km radius of intrahalocline eddies and allowing repeated sampling of individual features, in order to advance our understanding of the role of intrahalocline eddies in central Arctic Ocean dynamics, stratification, and the lateral transport of heat and freshwater.

Data availability. All datasets used in this study are publicly available, in compliance with the MOSAiC data policy. CTD Polarstern: Tippenhauer et al. (2023); ITPs: Toole et al. (2011); AOFBs: Stanton and Shaw (2023); ADCP Polarstern: Tippenhauer and Rex (2020)

Appendix A: Supplementary Figures for All Identified Eddies

This appendix presents the diagnostic figures for the remaining intrahalocline eddies (E1–E7), following the same notation and structure as in the main text. Figure A1 shows the eddy-centre detection using the MSV method. Figures A2–A3 provide the thermohaline and velocity cross-sections, and Figures A4-A5 show the vertical profiles of temperature, salinity, density, and velocity for each eddy.

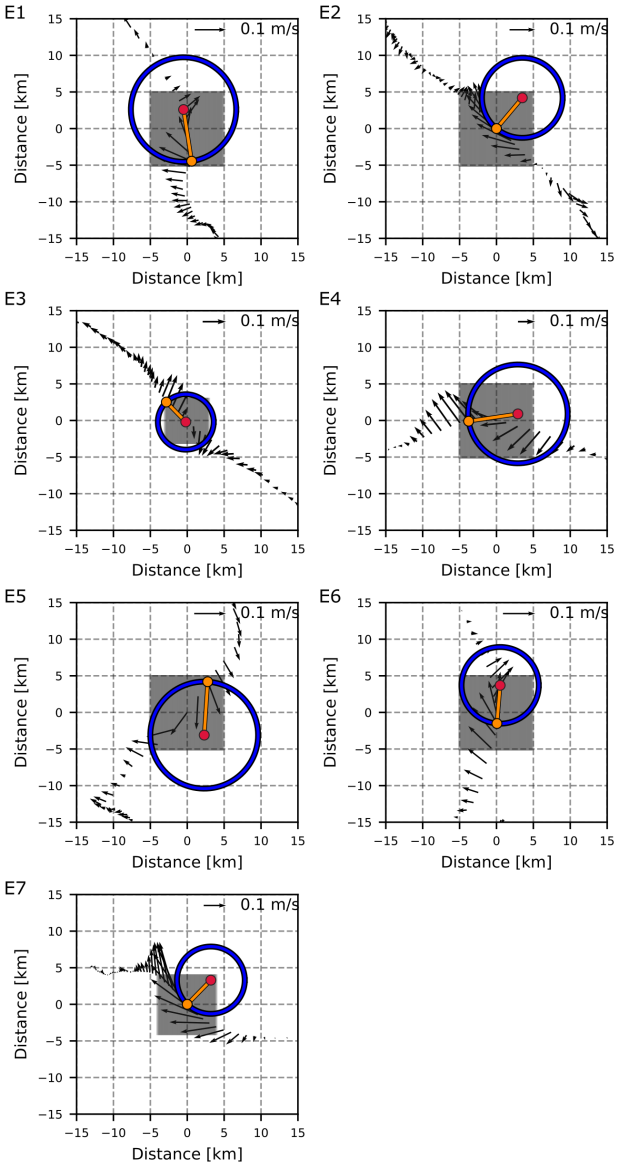

Figure A1. Velocity vectors of the eddies at the depth of maximum velocity. The grey area shows the grid used for the detection of the eddy centre, the red dot shows the estimated eddy centre using the methodology of Nencioli et al. (2008), the orange dot is the maximum azimuthal velocity (V_{max}) location and the orange line show the distance between the location of the absolute smallest azimuthal velocity (centre of the eddy) and V_{max}. The blue circle marks the inner part of the eddy.

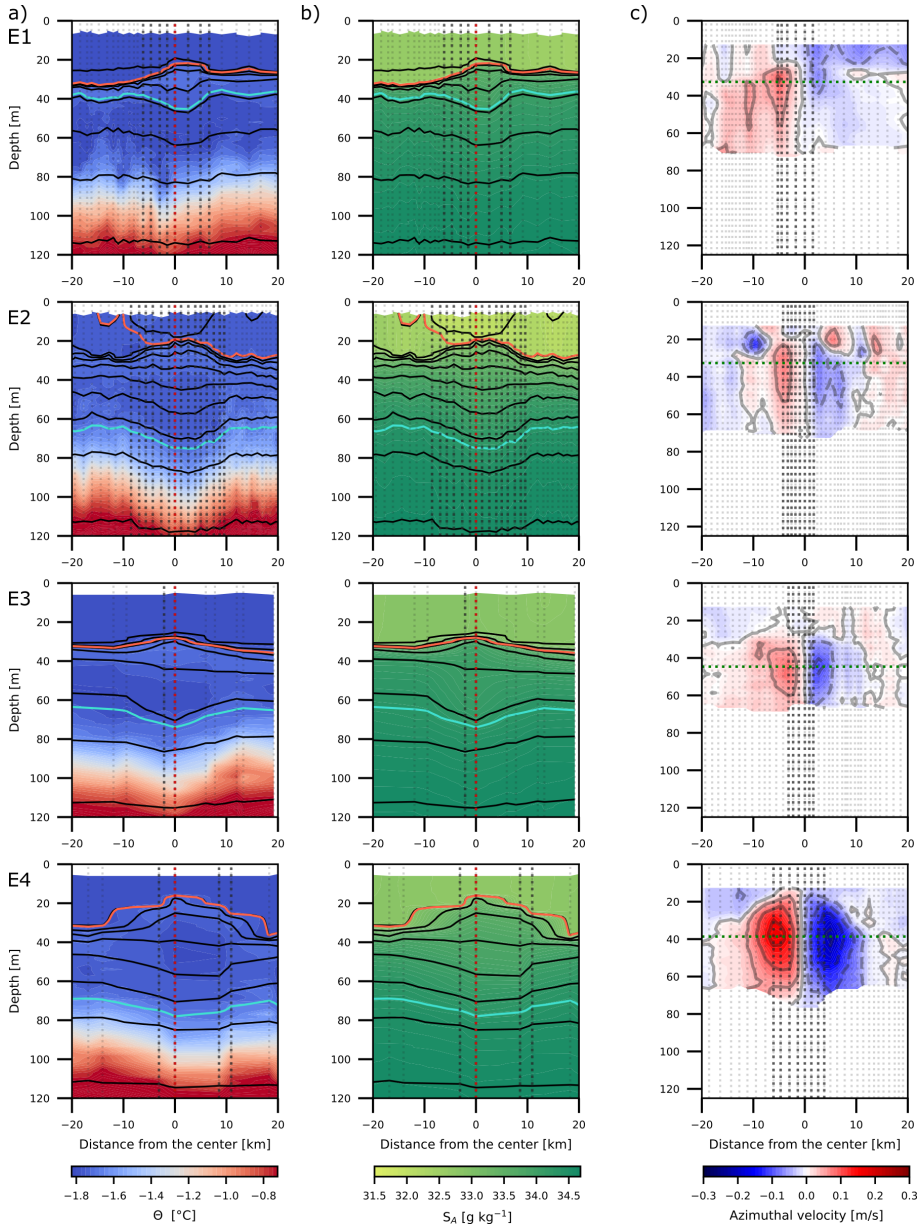

Figure A2. (a) Cross sections of conservative temperature (Θ) and (b) absolute salinity (g kg^{-1}) with isopycnals shown as black contours spaced every 0.25 kg m^{-3}; red and cyan contours indicate the upper and lower limits of the eddies, respectively, and the dashed vertical red line marks the central eddy profile. (f) Cross section of azimuthal velocity v_θ with velocity contours in grey every 0.05 ms^{-1}. The green dotted line indicates the depth of maximum velocity. The dotted vertical light grey lines in (a), (b) and (f) marker the measurement profiles, where the darker lines are the profiles inside the eddy in Figure A4.

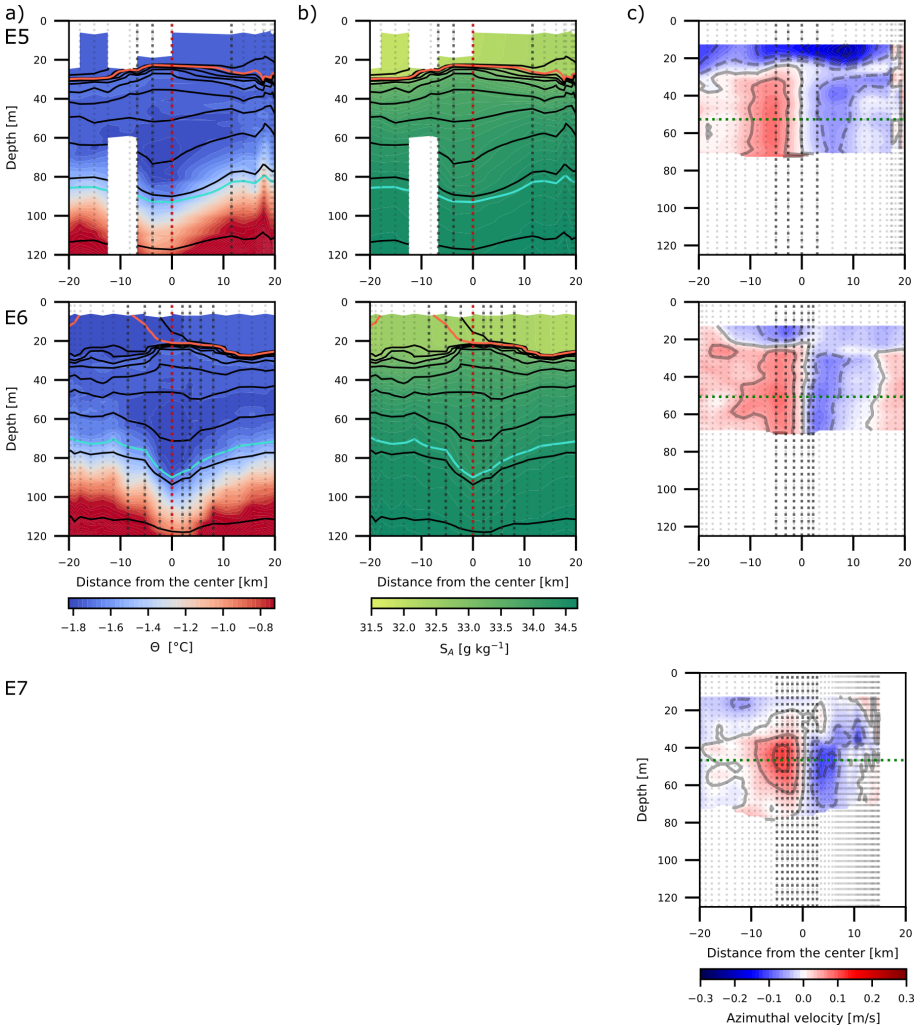

Figure A3. (a) Cross sections of conservative temperature (Θ) and (b) absolute salinity (g kg^{-1}) with isopycnals shown as black contours spaced every 0.25 kg m^{-3}; red and cyan contours indicate the upper and lower limits of the eddies, respectively, and the dashed vertical red line marks the central eddy profile. (f) Cross section of azimuthal velocity v_θ with velocity contours in grey every 0.05 ms^{-1}. The green dotted line indicates the depth of maximum velocity. The dotted vertical light grey lines in (a), (b) and (f) marker the measurement profiles, where the darker lines are the profiles inside the eddy in Figure A5.

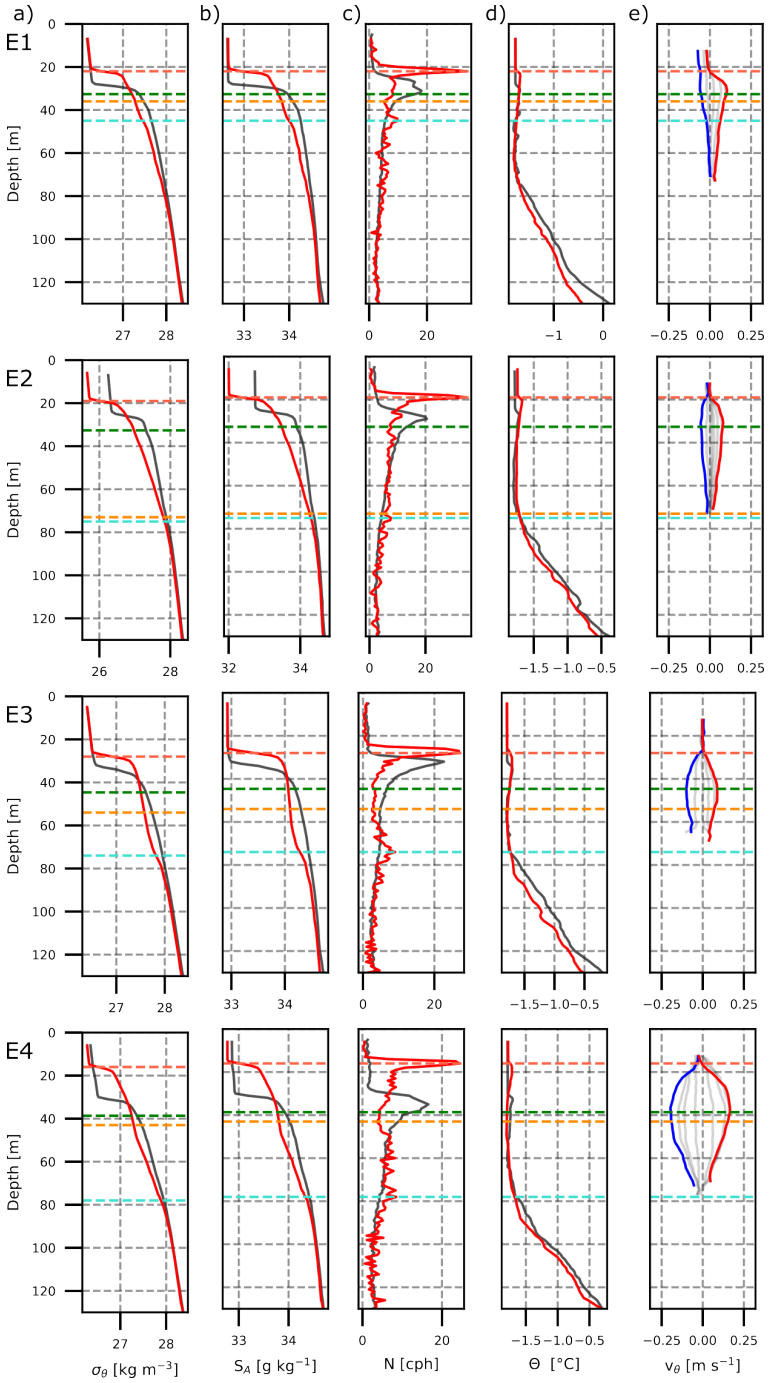

Figure A4. Vertical profiles of density (σ_θ) (a), absolute salinity (g kg^{-1}) (b), buoyancy frequency (N) (c), conservative temperature (Θ)(d), and azimuthal velocity (v_θ) (e). The red line shows the central profile, and the grey line shows the mean profiles at $\pm$ 20 km around the eddy, marked as dotted vertical light grey lines in Figure A2. Dashed horizontal lines show the top (red), the bottom (cyan), the maximum azimuthal velocity level (green) and the eddy core-centre depth (orange).

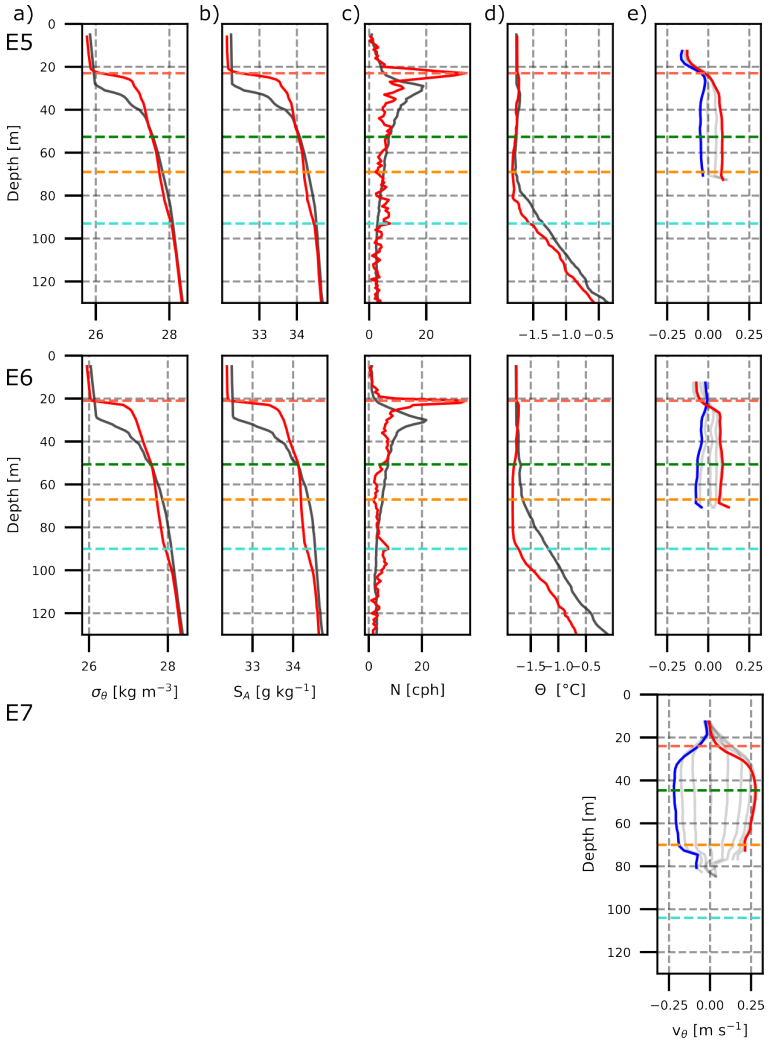

Figure A5. Vertical profiles of density (σ_θ) (a), absolute salinity (g kg^{-1}) (b), buoyancy frequency (N) (c), conservative temperature (Θ)(d), and azimuthal velocity (v_θ) (e). The red line shows the central profile, and the grey line shows the mean profiles at $\pm$ 20 km around the eddy, marked as dotted vertical light grey lines in Figure A3. Dashed horizontal lines show the top (red), the bottom (cyan), the maximum azimuthal velocity level (green) and the eddy core-centre depth (orange).

Author contributions. AQ, BR, CW and IK: conceptualisation of the study. Data processing: AQ, with assistance from BR and CW. Formal analysis: AQ with interactions from all co-authors. Preparation of the manuscript: All co-authors reviewed the manuscript and contributed to the writing and final editing.

Competing interests. At least one of the (co-)authors is a member of the editorial board of Ocean Science.

Acknowledgements. This research has been supported by the international Multidisciplinary drifting Observatory for the Study of the Arctic Climate (MOSAiC) with the tag MOSAiC20192020 (grant nos. AWI_PS122_00 and AFMOSAiC-1_00); the Alfred-Wegener-Institut Helmholtz-Zentrum für Polar- und Meeresforschung (Bremerhaven, Germany) through the Multidisciplinary Icebased Drifting Observatory (MIDO) infrastructure, the project AWI_OCEAN, and the project Sub-Mesoscale Dynamics and Nutrients (SMEDYN) within the INternational Science Program for Integrative Research in Earth Systems (INSPIRES); the EPICA project under the research theme MARE:N – Polarforschung/MOSAiC, funded by the German Federal Ministry for Education and Research (grant no. 03F0889A); the European Commission (EU H2020 grant no. 101003472, project Arctic PASSION); and the AROMA (Arctic Ocean mixing processes and vertical fluxes of energy and matter) project funded by the Research Council of Norway (grant no. 294396). Language editing assistance was provided using ChatGPT (OpenAI).

References

Aagaard, K. and Carmack, E. C.: The role of sea ice and other fresh water in the Arctic circulation, Journal of Geophysical Research: Oceans, 94, 14 485–14 498, 1989.

Acheson, D. J.: Elementary fluid dynamics, Oxford University Press, 1990.

Bush, J. W. and Woods, A. W.: An investigation of the link between lead-induced thermohaline convection and Arctic eddies, Geophysical research letters, 27, 1179–1182, 2000.

Carmack, E. C., Yamamoto-Kawai, M., Haine, T. W., Bacon, S., Bluhm, B. A., Lique, C., Melling, H., Polyakov, I. V., Straneo, F., Timmermans, M.-L., et al.: Freshwater and its role in the Arctic Marine System: Sources, disposition, storage, export, and physical and biogeochemical consequences in the Arctic and global oceans, Journal of Geophysical Research: Biogeosciences, 121, 675–717, 2016.

Castelão, G. and Johns, W.: Sea surface structure of North Brazil Current rings derived from shipboard and moored acoustic Doppler current profiler observations, Journal of Geophysical Research: Oceans, 116, 2011.

Castelão, G. P., Irber Jr, L. C., and Boas, A. B. V.: An objective reference system for studying rings in the ocean, Computers & Geosciences, 61, 43–49, 2013.

Chaigneau, A., Le Texier, M., Eldin, G., Grados, C., and Pizarro, O.: Vertical structure of mesoscale eddies in the eastern South Pacific Ocean: A composite analysis from altimetry and Argo profiling floats, Journal of Geophysical Research: Oceans, 116, 2011.

Chelton, D. B., Schlax, M. G., and Samelson, R. M.: Global observations of nonlinear mesoscale eddies, Progress in oceanography, 91, 167–216, 2011.

Cushman-Roisin, B. and Beckers, J.-M.: Introduction to geophysical fluid dynamics: physical and numerical aspects, vol. 101, Academic press, 2011.

Danilov, S., Sidorenko, D., Wang, Q., and Jung, T.: The finite-volume sea ice–ocean model (FESOM2), Geoscientific Model Development, 10, 765–789, 2017.

Della Penna, A. and Gaube, P.: Overview of (sub) mesoscale ocean dynamics for the NAAMES field program, Frontiers in Marine Science, 6, 384, 2019.

Dilmahamod, A. F., Aguiar-González, B., Penven, P., Reason, C., De Ruijter, W., Malan, N., and Hermes, J.: SIDDIES Corridor: A major east-west pathway of long-lived surface and subsurface eddies crossing the subtropical south Indian Ocean, Journal of Geophysical Research: Oceans, 123, 5406–5425, 2018.

Dugan, J., Mied, R., Mignerey, P., and Schuetz, A.: Compact, intrathermocline eddies in the Sargasso Sea, Journal of Geophysical Research: Oceans, 87, 385–393, 1982.

Fine, E. C., MacKinnon, J. A., Alford, M. H., and Mickett, J. B.: Microstructure observations of turbulent heat fluxes in a warm-core Canada Basin eddy, Journal of Physical Oceanography, 48, 2397–2418, 2018.

Hoppmann, M., Kuznetsov, I., Fang, Y.-C., and Rabe, B.: Mesoscale observations of temperature and salinity in the Arctic Transpolar Drift: a high-resolution dataset from the MOSAiC Distributed Network, Earth System Science Data, 14, 4901–4921, https://doi.org/10.5194/essd-14-4901-2022, 2022.

Jakobsson, M., Macnab, R., Mayer, L., Anderson, R., Edwards, M., Hatzky, J., Schenke, H. W., and Johnson, P.: An improved bathymetric portrayal of the Arctic Ocean: Implications for ocean modeling and geological, geophysical and oceanographic analyses, Geophysical Research Letters, 35, 2008.

Kikuchi, T., Hatakeyama, K., and Morison, J. H.: Distribution of convective lower halocline water in the eastern Arctic Ocean, Journal of Geophysical Research: Oceans, 109, 2004.

Kostianoy, A. and Belkin, I.: A survey of observations on intrathermocline eddies in the world ocean, in: Elsevier oceanography series, vol. 50, pp. 821–841, Elsevier, 1989.

Krishfield, R., Toole, J., Proshutinsky, A., and Timmermans, M.-L.: Automated ice-tethered profilers for seawater observations under pack ice in all seasons, Journal of Atmospheric and Oceanic Technology, 25, 2091–2105, 2008.

Kuzmina, N., Zhurbas, V., Rudels, B., Stipa, T., Paka, V., and Muraviev, S.: Role of eddies and intrusions in the exchange processes in the Baltic halocline, Oceanology, 48, 149–158, 2008.

Kuznetsov, I., Rabe, B., Androsov, A., Fang, Y.-C., Hoppmann, M., Quintanilla-Zurita, A., Harig, S., Tippenhauer, S., Schulz, K., Mohrholz, V., et al.: Dynamical reconstruction of the upper-ocean state in the central Arctic during the winter period of the MOSAiC expedition, Ocean Science, 20, 759–777, 2024.

Lenn, Y.-D., Fer, I., Timmermans, M.-L., and MacKinnon, J. A.: Mixing in the Arctic Ocean, in: Ocean mixing, pp. 275–299, Elsevier, 2022.

Li, X., Wang, Q., Danilov, S., Koldunov, N., Liu, C., Müller, V., Sidorenko, D., and Jung, T.: Eddy activity in the Arctic Ocean projected to surge in a warming world, Nature Climate Change, 14, 156–162, 2024.

MacKinnon, J. A., Simmons, H. L., Hargrove, J., Thomson, J., Peacock, T., Alford, M. H., Barton, B. I., Boury, S., Brenner, S. D., Couto, N., et al.: A warm jet in a cold ocean, Nature communications, 12, 2418, 2021.

Manley, T. and Hunkins, K.: Mesoscale eddies of the Arctic Ocean, Journal of Geophysical Research: Oceans, 90, 4911–4930, 1985.

McDougall, T. J. and Barker, P. M.: Getting started with TEOS-10 and the Gibbs Seawater (GSW) oceanographic toolbox, Scor/iapso WG, 127, 1–28, 2011.

McGillicuddy Jr, D. J.: Formation of intrathermocline lenses by eddy–wind interaction, Journal of Physical Oceanography, 45, 606–612, 2015.

McWilliams, J. C.: Submesoscale, coherent vortices in the ocean, Reviews of Geophysics, 23, 165–182, 1985.

McWilliams, J. C.: Vortex generation through balanced adjustment, Journal of Physical Oceanography, 18, 1178–1192, 1988.

Meneghello, G., Marshall, J., Lique, C., Isachsen, P. E., Doddridge, E., Campin, J.-M., Regan, H., and Talandier, C.: Genesis and decay of mesoscale baroclinic eddies in the seasonally ice-covered interior Arctic Ocean, Journal of Physical Oceanography, 51, 115–129, 2021.

Morison, J., Kwok, R., Peralta-Ferriz, C., Alkire, M., Rigor, I., Andersen, R., and Steele, M.: Changing arctic ocean freshwater pathways, Nature, 481, 66–70, 2012.

Müller, V., Wang, Q., Koldunov, N., Danilov, S., Sidorenko, D., and Jung, T.: Variability of eddy kinetic energy in the Eurasian Basin of the Arctic Ocean inferred from a model simulation at 1-km resolution, Journal of Geophysical Research: Oceans, 129, e2023JC020 139, 2024.

Nencioli, F., Kuwahara, V. S., Dickey, T. D., Rii, Y. M., and Bidigare, R. R.: Physical dynamics and biological implications of a mesoscale eddy in the lee of Hawai'i: Cyclone Opal observations during E-Flux III, Deep Sea Research Part II: Topical Studies in Oceanography, 55, 1252–1274, 2008.

Nicolaus, M., Perovich, D. K., Spreen, G., Granskog, M. A., von Albedyll, L., Angelopoulos, M., Anhaus, P., Arndt, S., Belter, H. J., Bessonov, V., et al.: Overview of the MOSAiC expedition: Snow and sea ice, Elem Sci Anth, 10, 000 046, 2022.

Nurser, A. and Bacon, S.: The rossby radius in the Arctic Ocean, Ocean Science, 10, 967–975, 2014.

Polyakov, I. V., Pnyushkov, A. V., Rember, R., Ivanov, V. V., Lenn, Y.-D., Padman, L., and Carmack, E. C.: Mooring-based observations of double-diffusive staircases over the Laptev Sea slope, Journal of Physical Oceanography, 42, 95–109, 2012.

Polyakov, I. V., Alkire, M. B., Bluhm, B. A., Brown, K. A., Carmack, E. C., Chierici, M., Danielson, S. L., Ellingsen, I., Ershova, E. A., Gårdfeldt, K., et al.: Borealization of the Arctic Ocean in response to anomalous advection from sub-Arctic seas, Frontiers in Marine Science, 7, 491, 2020.

Rabe, B., Karcher, M., Kauker, F., Schauer, U., Toole, J. M., Krishfield, R., Pisarev, S., Kikuchi, T., and Su, J.: Arctic Ocean basin liquid freshwater storage trend 1992–2012, Geophysical Research Letters, 41, 961–968, 2014.

Rabe, B., Heuzé, C., Regnery, J., Aksenov, Y., Allerholt, J., Athanase, M., Bai, Y., Basque, C., Bauch, D., Baumann, T. M., et al.: Overview of the MOSAiC expedition: Physical oceanography, Elem Sci Anth, 10, 00 062, 2022.

Rabe, B., Cox, C. J., Fang, Y.-C., Goessling, H., Granskog, M. A., Hoppmann, M., Hutchings, J. K., Krumpen, T., Kuznetsov, I., Lei, R., et al.: The MOSAiC Distributed Network: Observing the coupled Arctic system with multidisciplinary, coordinated platforms, Elem Sci Anth, 12, 00 103, 2024.

Rudels, B., Anderson, L., and Jones, E.: Formation and evolution of the surface mixed layer and halocline of the Arctic Ocean, Journal of Geophysical Research: Oceans, 101, 8807–8821, 1996.

Schulz, K., Büttner, S., Rogge, A., Janout, M., Hölemann, J., and Rippeth, T. P.: Turbulent mixing and the formation of an intermediate nepheloid layer above the Siberian continental shelf break, Geophysical Research Letters, 48, e2021GL092 988, 2021.

Schulz, K., Koenig, Z., Muilwijk, M., Bauch, D., Hoppe, C. J., Droste, E. S., Hoppmann, M., Chamberlain, E. J., Laukert, G., Stanton, T., et al.: The Eurasian Arctic Ocean along the MOSAiC drift in 2019–2020: an interdisciplinary perspective on physical properties and processes, Elementa: Science of the Anthropocene, 12, 2024.

Shakespeare, C. J.: Curved density fronts: Cyclogeostrophic adjustment and frontogenesis, Journal of Physical Oceanography, 46, 3193–3207, 2016.

Stanton, T. and Shaw, W.: Observations from Autonomous Ocean Flux Buoy 45 deployed at site L3 during the MOSAiC transpolar drift, Arctic Basin, 2019–2020, Arctic Data Center. DOI: https://dx. doi. org/10.18739/A26W96B3T, 2023.

Stanton, T. P., Shaw, W. J., and Hutchings, J. K.: Observational study of relationships between incoming radiation, open water fraction, and ocean-to-ice heat flux in the Transpolar Drift: 2002–2010, Journal of Geophysical Research: Oceans, 117, 2012.

Steele, M. and Boyd, T.: Retreat of the cold halocline layer in the Arctic Ocean, Journal of Geophysical Research: Oceans, 103, 10 419–10 435, 1998.

Thomas, L. N.: Formation of intrathermocline eddies at ocean fronts by wind-driven destruction of potential vorticity, Dynamics of Atmospheres and Oceans, 45, 252–273, 2008.

Timmermans, M.-L., Toole, J., Proshutinsky, A., Krishfield, R., and Plueddemann, A.: Eddies in the Canada Basin, Arctic Ocean, observed from ice-tethered profilers, Journal of Physical Oceanography, 38, 133–145, 2008.

Tippenhauer, S. and Rex, M.: Raw data of continuous VM-ADCP (vessel-mounted Acoustic Doppler Current Profiler) profile during PO-LARSTERN cruise PS122/1, https://doi.org/10.1594/PANGAEA.916092, 2020.

Tippenhauer, S., Vredenborg, M., Heuzé, C., Ulfsbo, A., Rabe, B., Granskog, M. A., Allerholt, J., Balmonte, J. P., Campbell, R. G., Castellani, G., et al.: Physical oceanography based on ship CTD during POLARSTERN cruise PS122, (No Title), 2023.

Toole, J. M., Krishfield, R. A., Timmermans, M.-L., and Proshutinsky, A.: The ice-tethered profiler: Argo of the Arctic, Oceanography, 24, 126–135, 2011.

Toole, J. M., Krishfield, R., O'Brien, J. K., Houk, A. E., Cole, S. T., et al.: Ice-Tethered Profiler observations: Vertical profiles of temperature, salinity, oxygen, and ocean velocity from an Ice-Tethered Profiler buoy system, (No Title), 2016.

von Appen, W.-J., Wekerle, C., Hehemann, L., Schourup-Kristensen, V., Konrad, C., and Iversen, M. H.: Observations of a submesoscale cyclonic filament in the marginal ice zone, Geophysical Research Letters, 45, 6141–6149, 2018.

Von Appen, W.-J., Baumann, T. M., Janout, M., Koldunov, N., Lenn, Y.-D., Pickart, R. S., Scott, R. B., and Wang, Q.: Eddies and the distribution of eddy kinetic energy in the Arctic Ocean, Oceanography, 35, 42–51, 2022.

Wang, J., Flierl, G. R., LaCasce, J. H., McClean, J. L., and Mahadevan, A.: Reconstructing the ocean's interior from surface data, Journal of Physical Oceanography, 43, 1611–1626, 2013.

Woodgate, R. A., Aagaard, K., Muench, R. D., Gunn, J., Björk, G., Rudels, B., Roach, A., and Schauer, U.: The Arctic Ocean boundary current along the Eurasian slope and the adjacent Lomonosov Ridge: Water mass properties, transports and transformations from moored instruments, Deep Sea Research Part I: Oceanographic Research Papers, 48, 1757–1792, 2001.

Zhao, M. and Timmermans, M.-L.: Vertical scales and dynamics of eddies in the Arctic Ocean's Canada Basin, Journal of Geophysical Research: Oceans, 120, 8195–8209, 2015.

Zhao, M., Timmermans, M.-L., Cole, S., Krishfield, R., Proshutinsky, A., and Toole, J.: Characterizing the eddy field in the A rctic O cean halocline, Journal of Geophysical Research: Oceans, 119, 8800–8817, 2014.

Zhao, M., Timmermans, M.-L., Krishfield, R., and Manucharyan, G.: Partitioning of kinetic energy in the Arctic Ocean's Beaufort Gyre, Journal of Geophysical Research: Oceans, 123, 4806–4819, 2018.